

INFORMATION TO USERS

This manuscript has been reproduced from the microfilm master. UMI films the text directly from the original or copy submitted. Thus, some thesis and dissertation copies are in typewriter face, while others may be from any type of computer printer.

The quality of this reproduction is dependent upon the quality of the copy submitted. Broken or indistinct print, colored or poor quality illustrations and photographs, print bleedthrough, substandard margins, and improper alignment can adversely affect reproduction.

In the unlikely event that the author did not send UMI a complete manuscript and there are missing pages, these will be noted. Also, if unauthorized copyright material had to be removed, a note will indicate the deletion.

Oversize materials (e.g., maps, drawings, charts) are reproduced by sectioning the original, beginning at the upper left-hand corner and continuing from left to right in equal sections with small overlaps. Each original is also photographed in one exposure and is included in reduced form at the back of the book.

Photographs included in the original manuscript have been reproduced xerographically in this copy. Higher quality 6" x 9" black and white photographic prints are available for any photographs or illustrations appearing in this copy for an additional charge. Contact UMI directly to order.

U·M·I

University Microfilms International
A Bell & Howell Information Company
300 North Zeeb Road, Ann Arbor, MI 48106-1346 USA
313/761-4700 800/521-0600

Order Number 1345318

**Optical characterization of lithium niobate thin film waveguides
sputtered on sapphire substrates**

Huang, Hung-Jia, M.S.

Rice University, 1991

U·M·I

**300 N. Zeeb Rd.
Ann Arbor, MI 48106**

RICE UNIVERSITY

**Optical Characterization of Lithium Niobate
Thin Film Waveguides Sputtered on Sapphire
Substrates**

by

Hung-Jia Huang

A THESIS SUBMITTED
IN PARTIAL FULFILLMENT OF THE
REQUIREMENTS FOR THE DEGREE

Master of Science

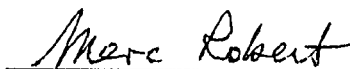
APPROVED, THESIS COMMITTEE:



Thomas A. Rabson, Chairman
Professor of Electrical and Computer
Engineering



Naomi J. Halas
Assistant Professor of Electrical and
Computer Engineering



Mark A. Robert
Associate Professor of Chemical
Engineering

Houston, Texas

July, 1990

Optical Characterization of Lithium Niobate Thin Film Waveguides Sputtered on Sapphire Substrates

Hung-Jia Huang

Abstract

Thin films of lithium niobate on various oriented sapphire substrates were fabricated by the rf sputtering method. Polarized He-Ne laser light with a wavelength of 6328 Å was successfully coupled into the optical waveguides by a rutile prism coupler. A description of the prism coupler used for this research is given. The guided modes excited by the prism coupler were observed and used to examine the optical properties of the waveguide. The refractive indices and thicknesses of various samples were calculated and tabulated. The birefringence observed in the films and x-ray diffraction studies have confirmed the polycrystalline nature of the films. The attenuation of the light propagating in various (zeroth- to second-order) waveguide modes was determined to be in the range of 1.1 to 1.3 ± 0.1 dB/cm.

Acknowledgments

I would like to express my sincere appreciation and gratitude to Dr. Thomas A. Rabson, my advisor, for his guidance and support in this endeavor. I would also like to thank the other members of my thesis committee, Dr. Naomi J. Halas and Dr. Mark A. Robert, for their valuable advice and assistance in completing the manuscript.

A great deal of thanks goes to many others for their helps in this work. First of all, thanks go to Tim Rost for making great films. Secondly, I would to thank Herman Chui for his help with building the prism coupler. Finally, I like to thank Barbara Stone for her assistance with the XRD work.

Furthermore, I would like to thank Mr. and Mrs. Wan-I Huang, my parents, and Wenbie L. Huang, my wife, for their encouragement and patience over the past years.

Contents

Abstract	ii
Acknowledgments	iii
List of Illustrations	v
List of Tables	ix
1 Introduction	1
2 Theory of Dielectric Planar Waveguides	4
2.1 Ray Optics of Planar Waveguides	4
2.1.1 Refraction and Reflection	4
2.1.2 Discrete Characteristics of Guided Modes	7
2.1.3 Birefringence	11
2.2 Eigenvalues of Maxwell's Equation	13
3 Prism Coupler	17
3.1 Why a Prism Coupler?	17
3.2 Principle of Operation of a Prism Coupler	18
3.3 Construction of the Prism Coupler and Mechanically Controlled Air Gap Profile	21
4 Results and Discussion	33
4.1 Fabrication of LiNbO ₃ Waveguides	33
4.2 Crystallinity of Thin-Film LiNbO ₃	34
4.3 Measurement of Refractive Index and Thickness	41

4.4	Measurement of Attenuation in the Waveguides	53
5	Conclusions	64
5.1	Prism Coupler	64
5.2	Crystallinity of the Sputtered Films	65
5.3	Refractive Index and Thickness	66
5.4	Attenuation	67
5.5	Future Research	68
5.5.1	Optical properties and fabrication techniques	68
5.5.2	Devices	69
5.5.3	Combination of Optical IC and Semiconductor IC	69
	Bibliography	70
	Appendix A	76
	Appendix B	79

Illustrations

2.1	Three-layer dielectric planar slab waveguide.	5
2.2	Incident wave refracted and reflected at an interface between two media with different indices of refraction.	5
2.3	Three-layer asymmetric slab waveguide. (a) Air radiation mode. (b) Substrate radiation mode. (c) Guided mode.	8
2.4	(a) The optical ray pattern within a slab waveguide. (b) The vertical and horizontal components of the wave vector \vec{k}	9
2.5	Birefringence in the rutile prism. Polarization parallel to the optic axis and perpendicular to the axis.	12
2.6	Field distribution of the waveguide.	15
3.1	Configuration of prism coupler.	19
3.2	Weak coupling interaction between the two evanescent fields within the air region.	20
3.3	Optimum gap profile	22
3.4	Two-prisms waveguide coupler.	23
3.5	Clamping system for the prism coupler.	24
3.6	Modified two-prism waveguide coupler.	27
3.7	Three-prism method.	28
3.8	Modified three-prism waveguide coupler.	28
3.9	Single-prism waveguide coupler.	30
3.10	Sarid's modified single-prism waveguide coupler.	30

3.11 Other modified configuration	32
4.1 XRD pattern of (001) sapphire substrate.	35
4.2 XRD pattern of LiNbO_3 film on (001) sapphire.	36
4.3 XRD pattern of (110) sapphire substrate.	37
4.4 XRD pattern of LiNbO_3 film on (110) sapphire.	38
4.5 Distortion of the lithium niobate unit cells near the interface due to lattice mismatch.	40
4.6 Relative intensity of reflected light vs. angle of incidence. TE modes for lithium niobate on (012) sapphire.	44
4.7 Relative intensity of reflected light vs. angle of incidence. TM modes for lithium niobate on (012) sapphire.	45
4.8 Relative intensity of reflected light vs. angle of incidence. TE modes for lithium niobate on (001) sapphire.	46
4.9 Relative intensity of reflected light vs. angle of incidence. TM modes for lithium niobate on (001) sapphire.	47
4.10 Relative intensity of reflected light vs. angle of incidence. TE modes for lithium niobate on (110) sapphire.	48
4.11 Relative intensity of reflected light vs. angle of incidence. TM modes for lithium niobate on (110) sapphire.	49
4.12 Optical power coupled into waveguide vs. angle of incidence.	50
4.13 Three-point parabola fitting method.	51
4.14 Characterization curve of the film sensitivity.	54
4.15 Surface-scattered light intensity of the TE modes of a LiNbO_3 waveguide on (001) sapphire measured by the photographic method as a function of distance along the waveguiding streak.	56

4.16	Surface-scattered light intensity of the TM modes of a LiNbO_3 waveguide on (001) sapphire measured by the photographic method as a function of distance along the waveguiding streak.	57
4.17	Surface-scattered light intensity of the TE modes of a LiNbO_3 waveguide on (110) sapphire measured by the photographic method as a function of distance along the waveguiding streak.	58
4.18	Surface-scattered light intensity of the TM modes of a LiNbO_3 waveguide on (110) sapphire measured by the photographic method as a function of distance along the waveguiding streak.	59
4.19	A 6328 \AA TM_2 mode was guided in the LiNbO_3 thin film. The rutile prism was clamped near the left edge of the waveguide. The guided streak was excited by the prism coupler and propagating from the left end to the right end of the waveguide.	60

Tables

4.1	Some parameters of lithium niobate and sapphire at room temperature and $\lambda = 6328 \text{ \AA}$. [22]	33
4.2	Sputtering conditions in the present experiment.	34
4.3	X-ray diffraction data.	40
4.4	Effective thicknesses and refractive indices corresponding to guided modes in the lithium niobate thin films deposited on sapphire.	51
4.5	Cutoff thicknesses corresponding to different modes. $n_f=2.2$ and $n_s=1.77$	53
4.6	Comparison of the attenuations measured by five research groups using different parameters in rf sputtering.	61

Chapter 1

Introduction

Since the early 1960's, when the laser was invented, light transmission and optical data processing have been topics of great interest. It was then learned that light transmission through air causes undesirable change in the light properties. Also, conventional optical components such as prisms, mirrors, lenses, and photodetectors are suitable for laboratory research, but not very useful for practical system applications. Thus, the concept of "integrated optics" [1-13] was developed. Today, optical computing and optical communication are two emerging fields of technology that are highly dependent on the development of integrated optical techniques. In this research we intend to study the optical, electro-optical, and acousto-optical properties [14,15] of thin films of lithium niobate rf-sputtered [16] on various substrates. A technique for producing high quality films of lithium niobate on silicon substrates has been developed by R. Baumann and T. Rost in the Electrical and Computer Engineering department at Rice University. Although the electrical properties of thin films of lithium niobate [17,18] are currently under thorough investigation for use in non-volatile electronic memory arrays [19,20], the application of this technique to integrated optics has not yet been explored. Lithium niobate has already been demonstrated to be a vital optical material in bulk and in thin diffused waveguides [13]. Lithium niobate is one of the most important passive optical materials and has drawn much attention in the area of integrated optics. This is mainly due to the following factors:

1. It is chemically very stable,
2. It is transparent in the visible and near IR region of the spectrum in its pure form,
3. Its electro-optic and acousto-optic coefficients are among the largest known.

Traditionally, metal in-diffused techniques and proton exchange have been used to make lithium niobate waveguides. Recently, significant progress has been reported in the area of rf sputtering lithium niobate on a variety of substrates. Griffel et al. [21] recently reported the lowest attenuation (less than 2 dB/cm) and the highest electro-optic coefficient (1.34×10^{-12} m/V) obtained so far for this type of film. They rf sputtered lithium niobate on an amorphous glass (Corning 7059) substrate. Hewig and Jain [22] also reported second harmonic generation in a lithium niobate film deposited on a sapphire substrate. Related research also reported that laser annealing significantly lowered the attenuation of the guide [23,24].

The on-going research project at Rice University on lithium niobate optical waveguides and components includes the following three stages of which the first part is the main concern of this thesis.

1. Evaluation of the refractive index, thickness, attenuation constant and preferred orientation of LiNbO_3 thin films rf sputtered on sapphire. By coupling the light beam into or out of the film [26,27], it is possible to determine the number of transverse electric (TE) and transverse magnetic (TM) modes present in the waveguide. Certainly, the appropriate devices for the evaluation have to be well designed in advance.
2. Measurement of other optical properties such as the linear electro-optical and the acousto-optical coefficients [14,15]. Electrodes will be photolithographically deposited on the top of the film. Both effects result in a periodic change of the index of refraction when a voltage is applied to the electrodes. This interacts

with the guided light to produce a phase shift which can then be detected by a photodiode and used to calculate the corresponding coefficients. The nonlinear effect of harmonic generation can be examined by coupling the laser light into the thin film and observing the frequency-doubled line in the spectrum of the light coupled out.

3. Fabrication of a channel waveguide either by molybdenum lift-off techniques or reactive plasma etching [25] of the lithium niobate. This allows one to build a phase modulator [6] and a Mach-Zehnder interferometer [13]. The Mach-Zehnder interferometer is of particular interest as a great number of integrated optical logic devices are based on this structure. The memory function of the films will be tested by using an intense optical beam to photorefractively change the refractive index of the film and reading the states of the film with a low energy beam reflected from the film. The change in magnitude and polarization will be measured to determine the index change in the film.

The results of the research described above will then be applied to building actual couplers, switches, modulators, doublers, and other optical processing elements.

Chapter 2

Theory of Dielectric Planar Waveguides

The dielectric planar slab waveguide [1-12] is the simplest light guide which is used to confine and guide the light in the devices and circuits of integrated optics. It is constructed by at least three layers as shown in Figure 2.1. The layer, which is usually a planar thin film, with the highest refractive index n_f is sandwiched between a cover and a substrate material with lower indices of refraction n_c and n_s ($n_f \geq n_s \geq n_c$). In most cases the cover material is air ($n_c = 1.0$). Since LiNbO_3 ($n_o \cong 2.3, n_e \cong 2.2$) is used as the waveguide in our work, a substrate with low refractive index, such as sapphire ($n \cong 1.77$), is required. If the film is to be made on a material with a refractive index higher than that of the film (e.g., $n(\text{silicon})=3.83$), a buffer layer (e.g., $n(\text{SiO}_2)=1.45$) must be formed between the waveguide and silicon substrate. The rest of this chapter is a review of planar waveguide theory.

2.1 Ray Optics of Planar Waveguides

The ray-optical approach is a fairly simple picture with great intuitive appeal, but it is not as complete and rigorous a description as that provided by electromagnetic field theory. However, the results derived ray-optically are in perfect agreement with the latter.

2.1.1 Refraction and Reflection

Figure 2.2 shows an interface separating two lossless, isotropic, homogeneous dielectric media of refractive indices n_1 and n_2 . A light beam is incident at an angle θ_1 between

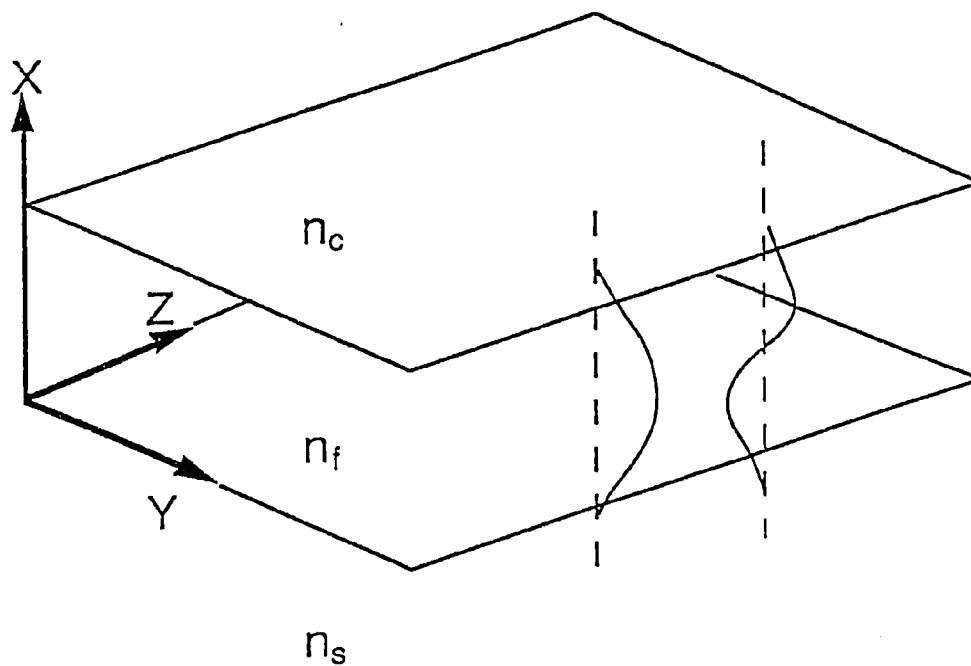


Figure 2.1 Three-layer dielectric planar slab waveguide.

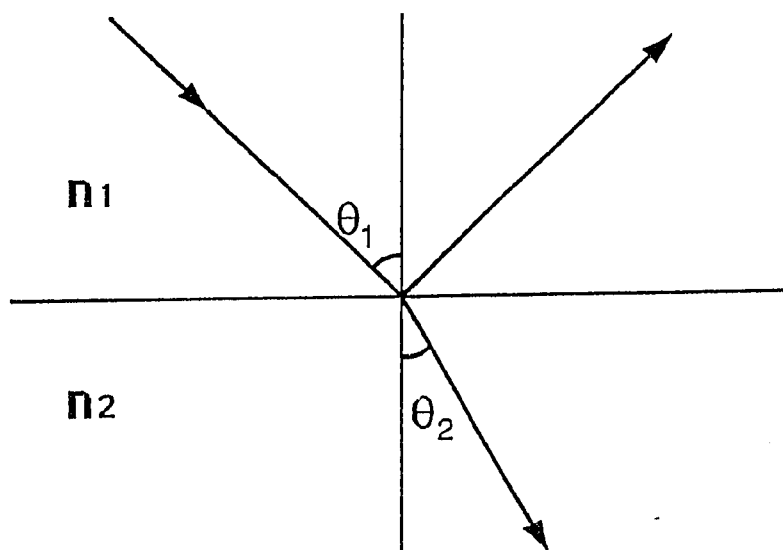


Figure 2.2 Incident wave refracted and reflected at an interface between two media with different indices of refraction.

the beam path and the normal to the interface. The refraction angle θ_2 is given by Snell's law

$$n_1 \sin \theta_1 = n_2 \sin \theta_2. \quad (2.1)$$

The amplitude of reflection coefficient is more complicated and depends not only on the index of refraction and the angle of incidence but on the polarization of the light. The relationships are given by Fresnel's formulae [6]. For TE waves, in which the electric field is perpendicular to the plane of incidence, we have

$$R_{TE} = \frac{n_1 \cos \theta_1 - n_2 \cos \theta_2}{n_1 \cos \theta_1 + n_2 \cos \theta_2}. \quad (2.2)$$

For TM waves, in which the electric field is parallel to the plane of incidence, we have

$$R_{TM} = \frac{n_2 \cos \theta_1 - n_1 \cos \theta_2}{n_2 \cos \theta_1 + n_1 \cos \theta_2}. \quad (2.3)$$

R_{TE} and R_{TM} are the reflection coefficients corresponding to TE and TM waves. Examining these equations, we learn that as soon as the incident angle is greater than the angle θ_c , which is given by $\theta_c = \sin^{-1}(n_2/n_1)$ and is the so-called *critical angle*, total reflection occurs. Since R is complex valued, a phase shift is thus imposed on the reflected light. The phase shifts ϕ_{TE} and ϕ_{TM} corresponding to the two polarization states are given by

$$\tan \phi_{TE} = \frac{\sqrt{n_1^2 \sin^2 \theta_1 - n_2^2}}{n_1 \cos \theta_1} \quad (2.4)$$

for TE waves, and

$$\tan \phi_{TM} = \frac{n_1^2}{n_2^2} \frac{\sqrt{n_1^2 \sin^2 \theta_1 - n_2^2}}{n_1 \cos \theta_1} \quad (2.5)$$

for TM waves. The phase shifts ϕ_{TE} and ϕ_{TM} are named *Goos-Hänchen* shifts [6].

Consider now the three-layer asymmetric slab waveguide as shown in Figure 2.3. In general, we have $n_f > n_s > n_c$. Let us increase θ_1 gradually from zero. When the light is coming in, for example, from the air layer and θ_1 is small, the incident light can penetrate through the film layer and propagate into the substrate as shown in Figure 2.3(a). In this case, the wave travels freely in all three media and corresponds to the *air radiation mode* or *air mode*. As θ_1 gets larger and eventually exceeds the critical angle $\sin^{-1}(n_c/n_f)$ of the air-film interface as shown in Figure 2.3(b), the light wave is totally reflected at the film-air boundary. The light can no longer propagate freely in air and its energy in the film radiates into the substrate only. This therefore corresponds to the *substrate radiation mode* or *substrate mode*. Lastly, when θ_1 is larger than the critical angle $\sin^{-1}(n_s/n_f)$ of the film-substrate interface, as shown in Figure 2.3(c), the light wave is totally reflected not only at the film-air boundary but also at the film-substrate one. We now can see that the energy flow of light is completely confined within the waveguide. Since the light wave is trapped in the waveguide, it is then categorized as a *guided mode*. From the ray-optical point of view, the physical picture of the guided light is that of light propagating in a zig-zag fashion in the film and bouncing back and forth between the two interfaces.

2.1.2 Discrete Characteristics of Guided Modes

Figure 2.4(a) corresponds to the optical ray pattern within a multimode slab waveguide. A plane wave can be represented by its wave vector \vec{k} travelling at an angle θ_m with respect to the z direction. As shown in Figure 2.4(b), \vec{k} can then be decomposed into a z direction propagation constant β and a x direction propagation constant

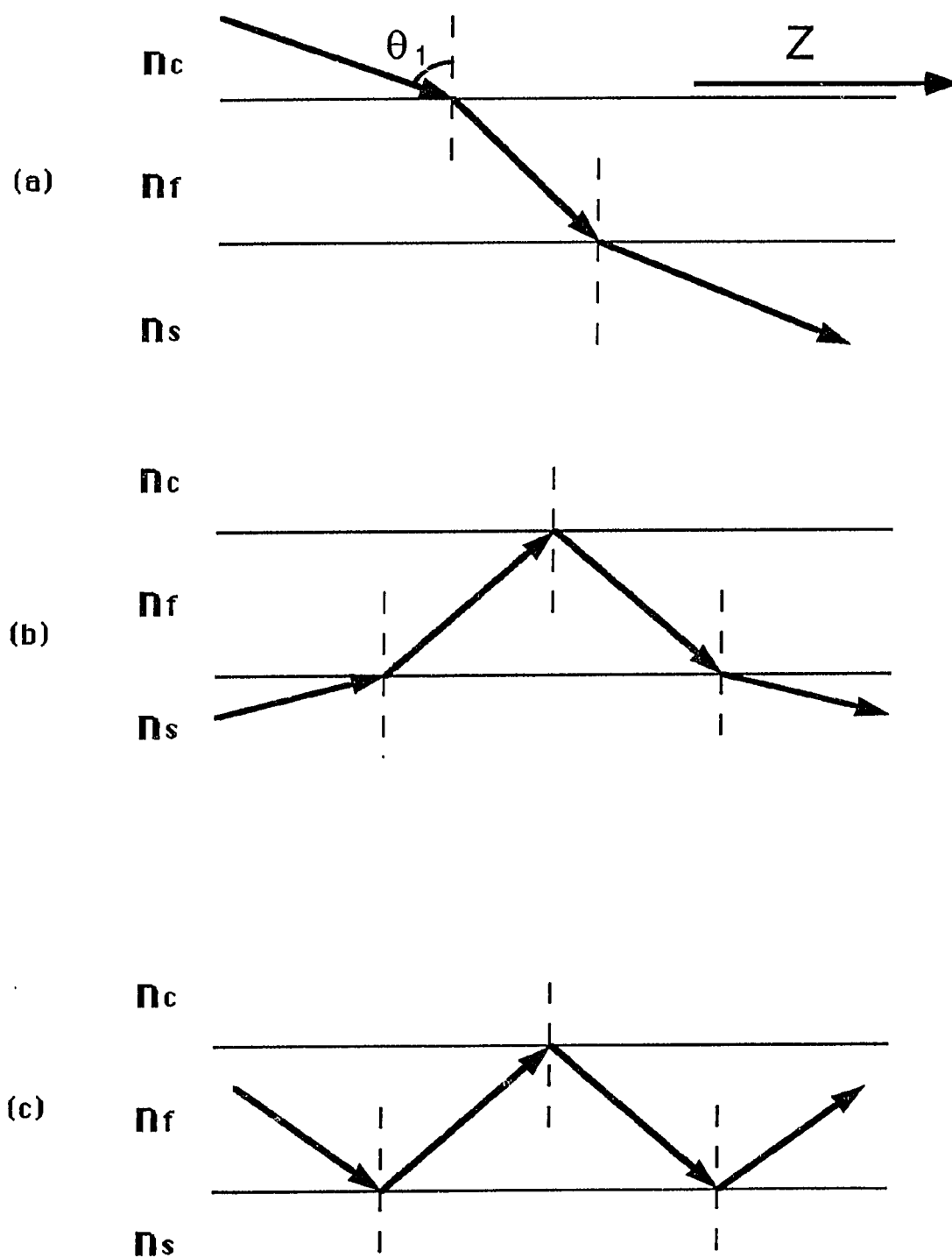
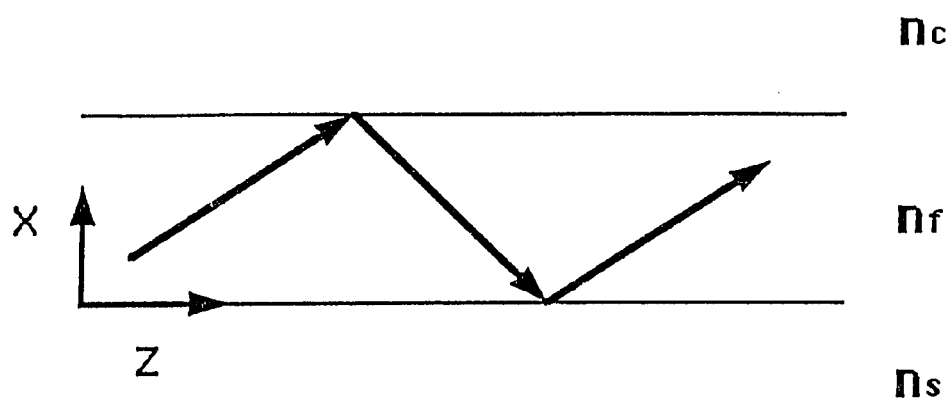
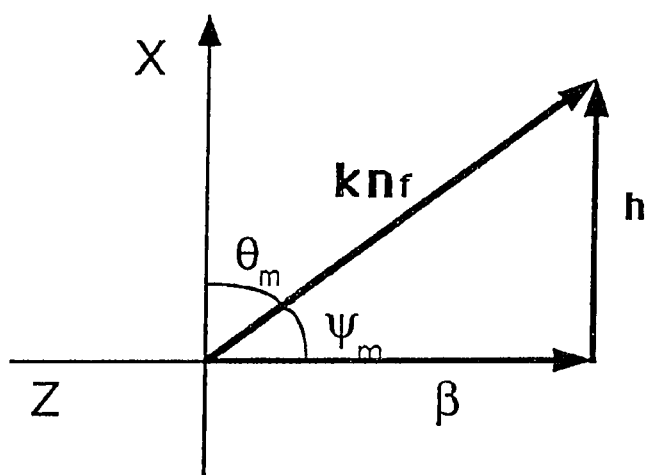


Figure 2.3 Three-layer asymmetric slab waveguide. (a) Air radiation mode. (b) Substrate radiation mode. (c) Guided mode.



(a)



(b)

Figure 2.4 (a) The optical ray pattern within a slab waveguide. (b) The vertical and horizontal components of the wave vector \vec{k} .

h . From Figure 2.4(b), we can get the relationship relating the three propagation constants,

$$\beta^2 + h^2 = k^2 n_f^2, \quad (2.6)$$

as well as the equation for calculating the angle,

$$\psi_m = \tan^{-1} \frac{h}{\beta_m}, \quad (2.7)$$

where ψ_m and β_m are associated with the m -th mode. Equation 2.6, which can also be derived from Maxwell's equation, is the mode condition of propagation in the waveguide. The solution of Maxwell's equation subject to the boundary conditions requires that only a finite number of discrete values of β are allowed provided the guide is thick enough to support the modes. This restriction on β can be visualized simply by the ray-optical approach. In order to keep a constant phase for the plane wave assumption and avoid attenuation of optical energy due to destructive interference as the wave propagates through the guide, the total phase shift for a point on a wavefront which travels from an interface to the second interface and back again to the first one is required to be a multiple of 2π . The above statement gives the following condition,

$$2kn_f t \sin \psi_m - 2\phi_{fc} - 2\phi_{fs} = 2m\pi, \quad (2.8)$$

where t is the thickness of the waveguide, ϕ_{fc} and ϕ_{fs} are the phase shifts due to total internal reflection at the film-cover and the film-substrate interfaces respectively (given in equations 2.4 and 2.5), and m is the mode number. For given n_c, n_f, n_s, m and t, ψ_m can be calculated and a set of discrete numbers is thus obtained. From

Figure 2.3(b), the propagation constant β_m corresponding to each allowed mode is given by

$$\beta_m = kn_f \sin \theta_m = kn_f \cos \psi_m. \quad (2.9)$$

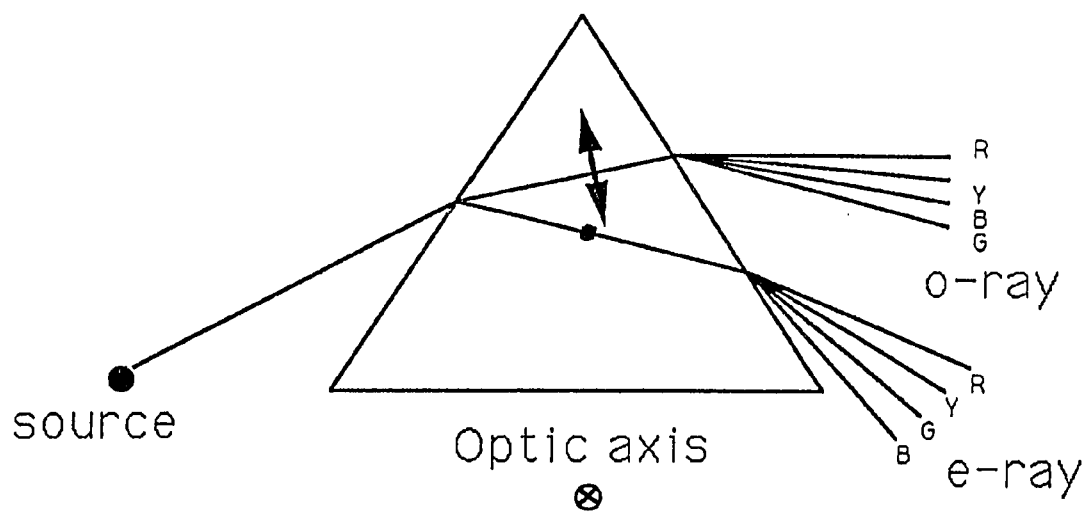
Since the velocity v of the light propagating in the z direction is equal to $c(\frac{k}{\beta})$, we can then define an effective index of refraction for the waveguide as

$$n_{eff} = \frac{c}{v} = \frac{\beta}{k}. \quad (2.10)$$

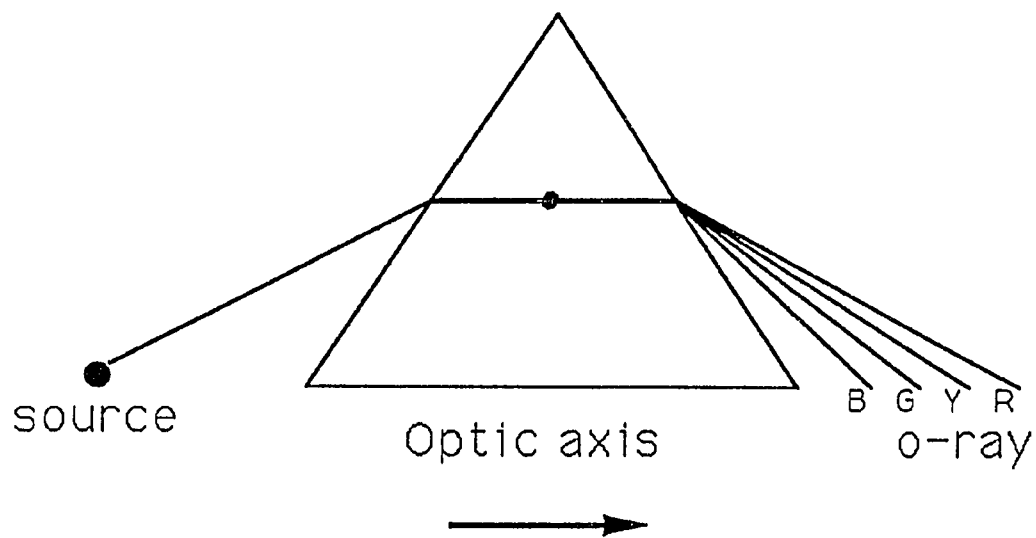
This is one of the most important optical parameters of thin film waveguides in which we are interested.

2.1.3 Birefringence

The phenomena of refraction described in section 2.1.1 assumed that the media were all isotropic. However, most crystals are anisotropic and birefringence (double refraction) [10] will be observed when a light beam passes through an anisotropic crystal. This effect is explained by assuming that the crystal has two different indices of refraction such that the light could be refracted into two different directions as it entered the crystal. The indices of birefringence are referred to as *ordinary* (n_o) and *extraordinary* (n_e). For an uniaxial crystal, if $n_e > n_o$, the crystal is called positive; otherwise, it is negative. LiNbO_3 ($n_e = 2.19$ and $n_o = 2.28$ at $\lambda = 0.80\mu m$), for example, is a negative uniaxial crystal, while rutile, with $n_e = 2.903$ and $n_o = 2.616$ at $\lambda = 0.589 \mu m$, is positive. Of particular interest, the birefringence of rutile is shown in Figure 2.5, which demonstrates the relation between the polarization of the incident beam and the direction of the optic axis in the crystal.



(a)



(b)

Figure 2.5 Birefringence in the rutile prism. Polarization parallel to the optic axis and perpendicular to the axis.

2.2 Eigenvalues of Maxwell's Equation

An equivalent mathematical description of a mode is that it is an electromagnetic field which is a solution (eigenvalue) of Maxwell's wave equation

$$\nabla^2 \vec{E}(\vec{r}, t) = \left[\frac{n^2(\vec{r})}{c^2} \right] \frac{\partial^2 \vec{E}(\vec{r}, t)}{\partial t^2}, \quad (2.11)$$

where \vec{E} is the electric field vector, $n(\vec{r})$ is the refractive index, \vec{r} is the radius vector, and c is the speed of light in vacuum. For a monochromatic wave, the solutions of equation 2.11 have the form

$$\vec{E}(\vec{r}, t) = \vec{E}(\vec{r}) e^{i\omega t}, \quad (2.12)$$

where ω is the angular frequency. Substituting equation 2.12 into equation 2.11, we have

$$\nabla^2 \vec{E}(\vec{r}) + k^2 n^2(\vec{r}) \vec{E}(\vec{r}) = 0, \quad (2.13)$$

where $k \equiv \omega/c$. For convenience, a uniform plane wave propagating in the z direction is assumed, i.e., $\vec{E}(\vec{r}) = \vec{E}(x, y) e^{-i\beta z}$, β being a propagation constant in the z direction; then equation 2.13 becomes

$$\frac{\partial^2 E(x, y)}{\partial x^2} + (k^2 n_i^2 - \beta^2) E(x, y) = 0, \quad (2.14)$$

where $i=c, f$ and s corresponding to region C, F and S respectively and $E(x, y)$ is a Cartesian component of the mode function $\vec{E}(x, y)$. We have dropped the $\partial^2 E / \partial y^2$ term in the above equation, since the waveguide is assumed infinite in the y direction.

The solutions of equation 2.14 are either sinusoidal or exponential functions of x in each of the regions, depending on whether $(k^2 n_i^2 - \beta^2)$ is positive or negative. The boundary conditions require both $E(x, y)$ and $\partial E(x, y)/\partial x$ to be continuous across every interface. Assuming $n_f > n_s > n_c$, we can qualitatively draw the possible modes as shown in Figure 2.6. When $\beta > kn_f$, $E(x)$ is exponential in all regions and the only possible mode shape is shown as Figure 2.6(a). This is physically non-realizable since the field increases exponentially in the cover and substrate layer. Modes (b) and (c) represent zeroth- and first-order guided modes which can be supported for the value of β in between kn_f and kn_s . If $kn_s > \beta > kn_c$, substrate modes as shown in Figure 2.6(d) will result. When β is less than kn_c , the solutions for $E(x)$ are sinusoidal in all three regions and thus the wave is freely travelling in all space. They are therefore referred to as air modes. Figure 2.6 has been discussed in great detail by Yariv and Yeh [10].

Solving equation 2.14 and imposing the appropriate boundary conditions, we obtain the so-called *mode conditions*

$$\tan ht = \frac{p + q}{h(1 - pq/h^2)} \quad (2.15)$$

for TE modes, and

$$\tan ht = \frac{h(\bar{p} + \bar{q})}{h^2 - \bar{p}\bar{q}} \quad (2.16)$$

for TM modes, where

$$\begin{aligned} h &= \sqrt{n_f^2 k^2 - \beta^2}, \\ q &= \sqrt{\beta^2 - n_c^2 k^2}, \\ p &= \sqrt{\beta^2 - n_s^2 k^2}, \\ \bar{p} &= pn_f^2/n_s^2, \\ \bar{q} &= qn_f^2/n_c^2. \end{aligned} \quad (2.17)$$

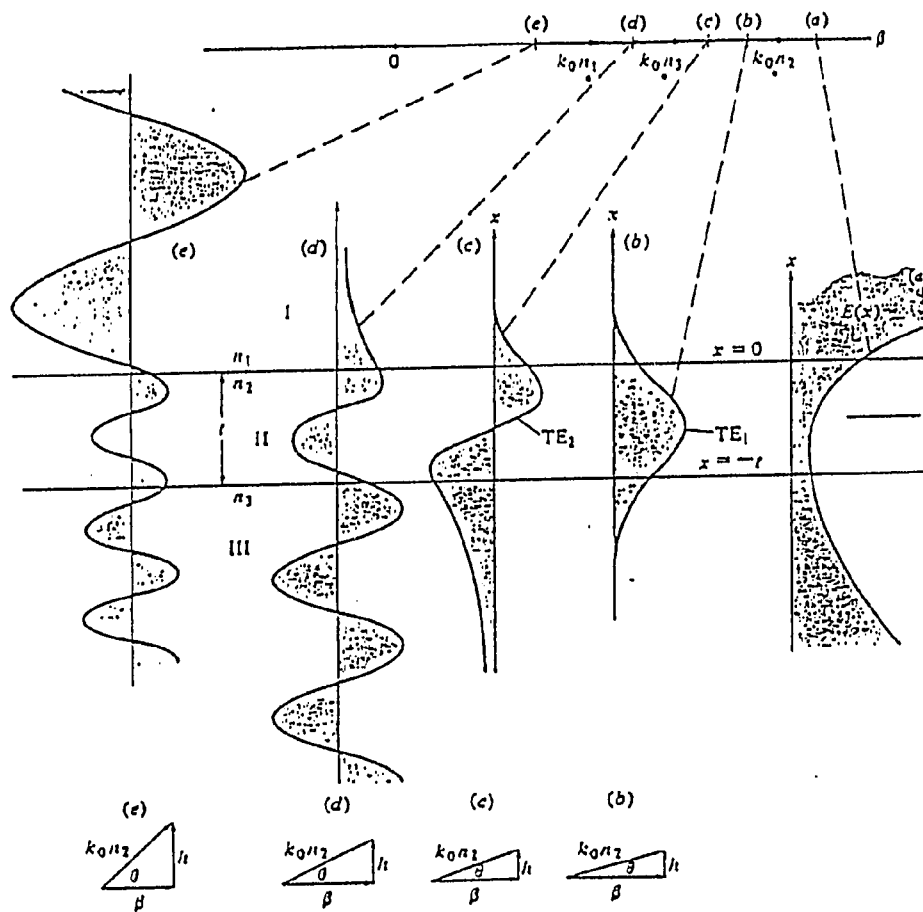


Figure 2.6 Field distribution of the waveguide. [10]

This set of equations is mathematically equivalent to equation 2.8 which was derived by ray optics in the previous section. Given a set of indices n_c, n_f and n_s of a slab waveguide, each equation yields in general a finite number of β 's provided that the thickness t is large enough. According to the mode conditions, cutoff values of t/λ for TE and TM modes are given, respectively, by equation (11.2-14) in Ref. [10]. In practice, the refractive indices n_c and n_s are well-known before the guide is fabricated. Also, parameter k can be calculated as soon as we determine the light source to be used. Now, if two modes can be measured, i.e., two different values of β are obtained, the refractive index n_f as well as the thickness t of the guide can then be determined simultaneously. Of course, if more than two modes are observed, the solutions are over-determined. The extra data can be used to compute the standard deviation. A computer program, given two β 's as the input, has been written for calculating n_f and t . Means of measuring a set of propagation constants is then needed for getting the input data.

Chapter 3

Prism Coupler

3.1 Why a Prism Coupler?

In order to evaluate the propagation characteristics of the dielectric thin-film waveguide, various beam-film couplers, namely end-fire couplers [5,6], prism couplers [26-56] and grating couplers [5,6], have been utilized for converting the energy of a light beam into one mode (or multimodes) guided by the thin film layer. Since the thickness of the thin film which we are dealing with is typically less than $1\ \mu m$, observation of the optical mode guided by such thin films utilizing the end-fire coupler cannot be accomplished without a finely-adjustable experimental set-up. Although the grating coupler is widely used in optical integrated circuits, however, it is not very easy to make and the coupling efficiency is not as high as that of a prism coupler. In addition to the ability to avoid precise optical focusing and critical alignment which are necessary for the end-fire method, the possibility of a much higher optimum coupling efficiency than that of the grating coupler is the main reason for choosing the prism coupler as the primary coupling tool.

Theoretically, as was calculated by Tien and Ulrich [30,31], the coupling efficiency of a frequently used coupler configuration with a right-angle prism and a uniform air gap between the prism base and the film was predicted to have a maximum value of 80.1 % for Gaussian input beams. However, it is able to approach optimum value of 100 % coupling if the optimum air-gap profile is closely approached.

3.2 Principle of Operation of a Prism Coupler

In its simplest configuration, the prism coupler makes use of a high-index prism placed in close proximity to a planar dielectric waveguide as shown in Figure 3.1.

When a plane wave is incident upon the bottom surface of the prism at an angle θ exceeding the critical angle ($\theta_c = \sin^{-1}(\frac{n_a}{n_p})$), the superposition of the incident wave and the totally reflected wave yield a standing wave above the prism-air interface and the field is propagating in the direction parallel to the interface. The entire field can thus be regarded as a mode propagating along the z direction. Consider now a guided surface wave travelling in the thin film waveguide of thickness t ; the field inside the film is sinusoidal (standing wave), which is decaying exponentially outside the film. We can expect that there is weak interaction between these modes through the two evanescent fields within the air region as shown in Figure 3.2. This implies that optical energy can be transferred back and forth via an *optical tunneling effect*. The energy interchange of the weakly coupled mode is complete if these two modes are phase-matched. Mathematically speaking, the condition

$$kn_p \sin \theta = \beta_m \quad (3.1)$$

should be fulfilled, where k is the wave vector in a vacuum, n_p is the refractive index of the prism, and β_m is the propagation constant of the m -th mode. A complete interchange of optical energy can then be achieved if the coupling length L is given by

$$\kappa L = \frac{\pi}{2}, \quad (3.2)$$

where κ is the coupling coefficient between the two modes. The coupling coefficient can be changed by adjusting the thickness of the air gap. However, because of the effect of the beam profile, only 80.1 %, in the best case, of the optical energy can be transferred in the case of a uniform air gap and a Gaussian beam profile. This was

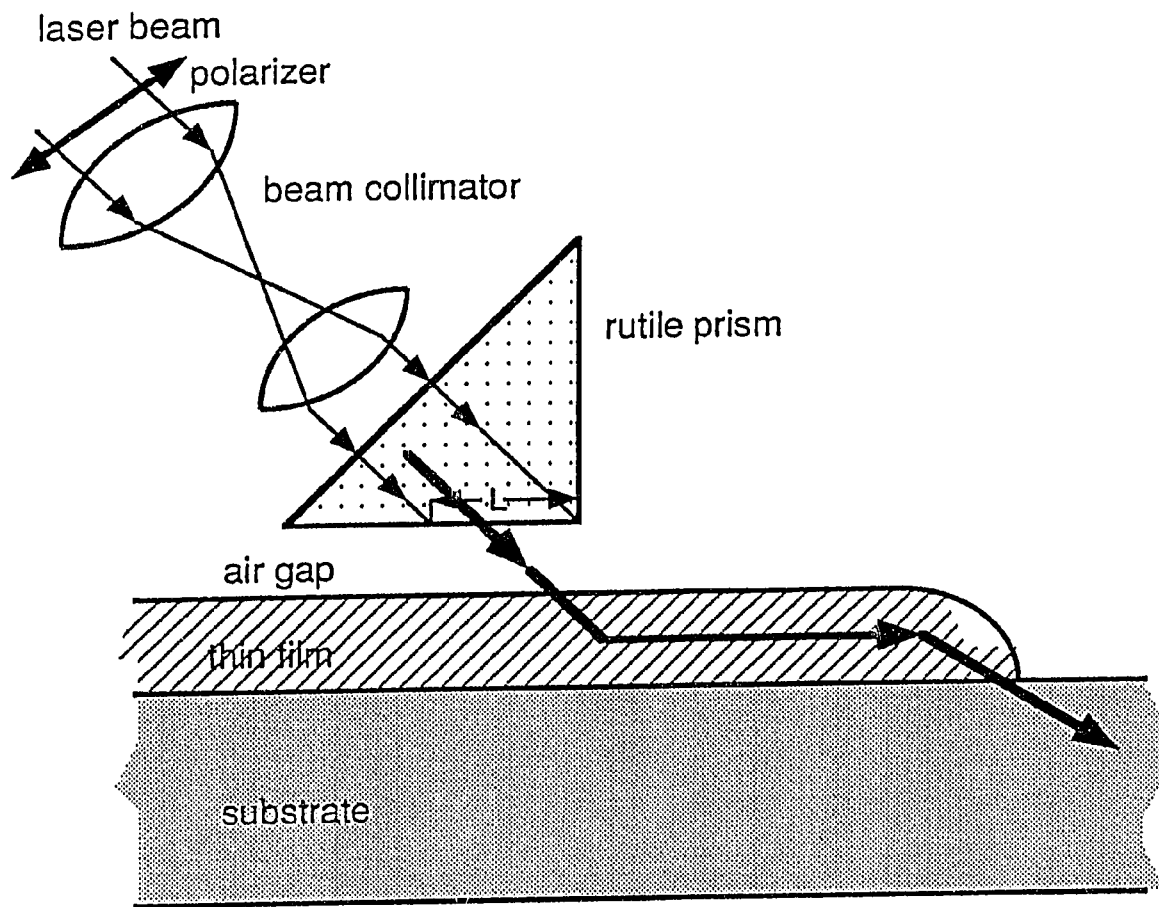


Figure 3.1 Configuration of prism coupler.

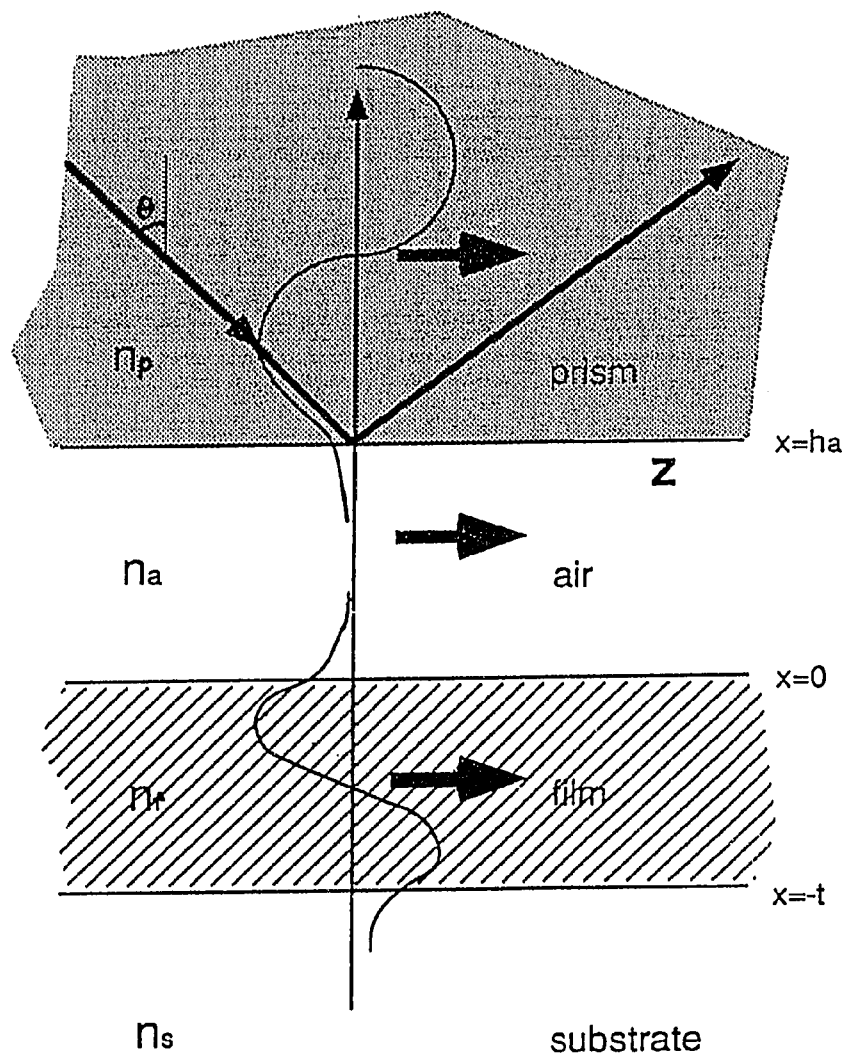


Figure 3.2 Weak coupling interaction between the two evanescent fields within the air region.

reported by Ulrich who also calculated the air-gap profile required for obtaining 100 % coupling efficiency by assuming plane waves were travelling in the media. Referring to Figure 3.3, the optimum gap profile under the condition of weak coupling is given by [32]

$$S_{opt}(x) = k^{-1}(\beta^2 - n_g^2)^{-1/2} \ln[h_{opt}^{-1}(x)], \quad (3.3)$$

where $k = 2\pi/\lambda$, λ is the free space wavelength, β is the propagation constant in the waveguide, n_g is the refractive index of the gap material (air), and $h_{opt}(x)$ is the optimum spatial dependence of the coupling strength. The way to calculate the parameter $h_{opt}(x)$ is shown in Reference [30-32]. If a Gaussian beam is used, the optimum gap profile can be simulated by a linearly tapered gap in practice. The closer an actual gap profile conforms to the optimum profile, the more closely the coupling efficiency approaches the theoretical limit of 100 %.

3.3 Construction of the Prism Coupler and Mechanically Controlled Air Gap Profile

In this work, various configurations for a prism-waveguide coupler have been tried for determining the most versatile and suitable one for the first phase of our research project mentioned in chapter 1.

Figure 3.4 shows the construction of the two-prism waveguide coupler. Both prisms are held individually by a "C" clamp, as shown in Figure 3.5, at their triangular faces, so that the disadvantage of the traditional method of clamping the prism directly at one of the corners can be avoided. The waveguide is then pressed against the base of the prism with the right angle touching the surface of the waveguide. The adjustable pressure system is mainly an air cylinder controlled by a push-pull switching valve and a pressure regulator. Most of the conventional devices we tried, such as a mechanical screw, are not capable of monitoring the applied pressure, there-

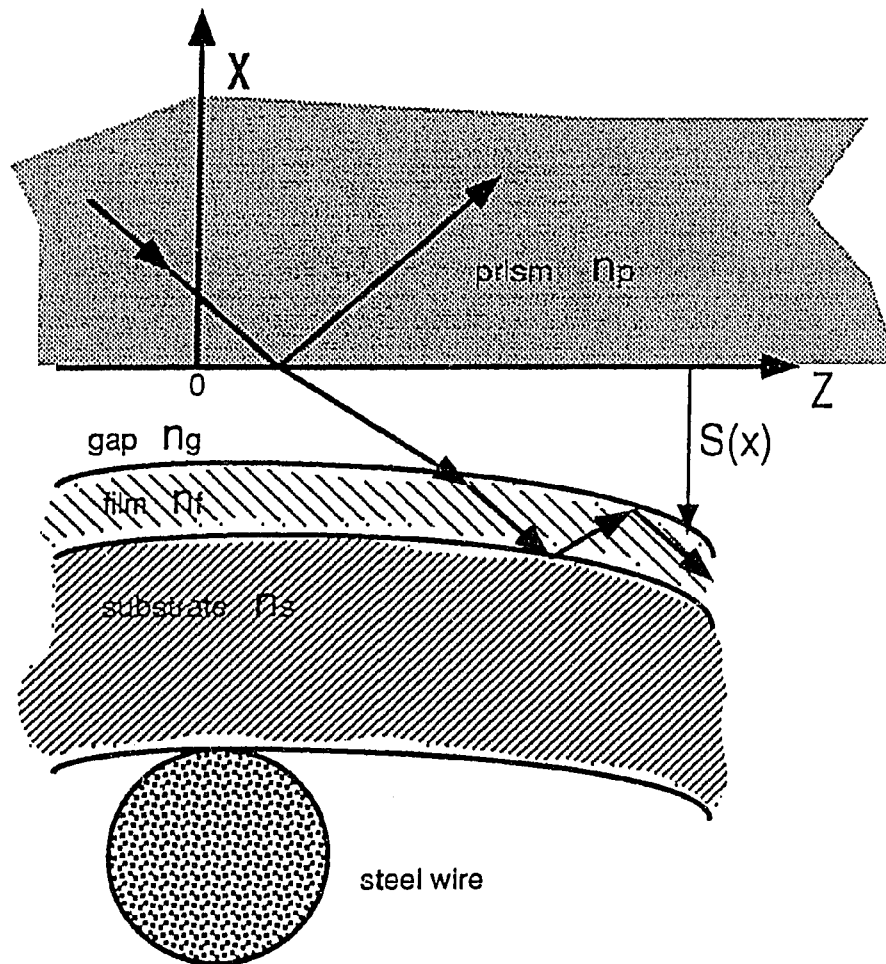


Figure 3.3 Optimum gap profile

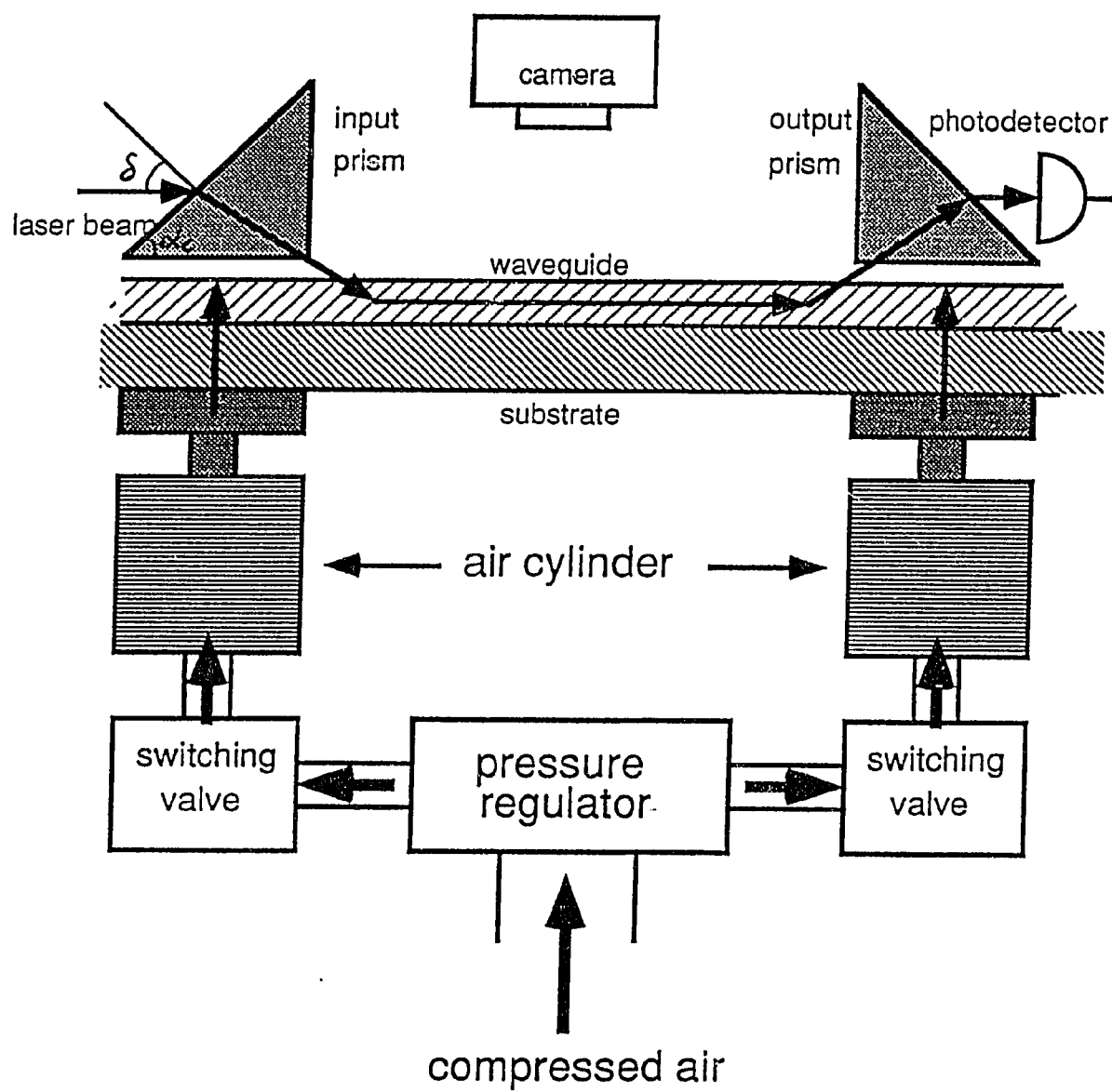


Figure 3.4 Two-prisms waveguide coupler.

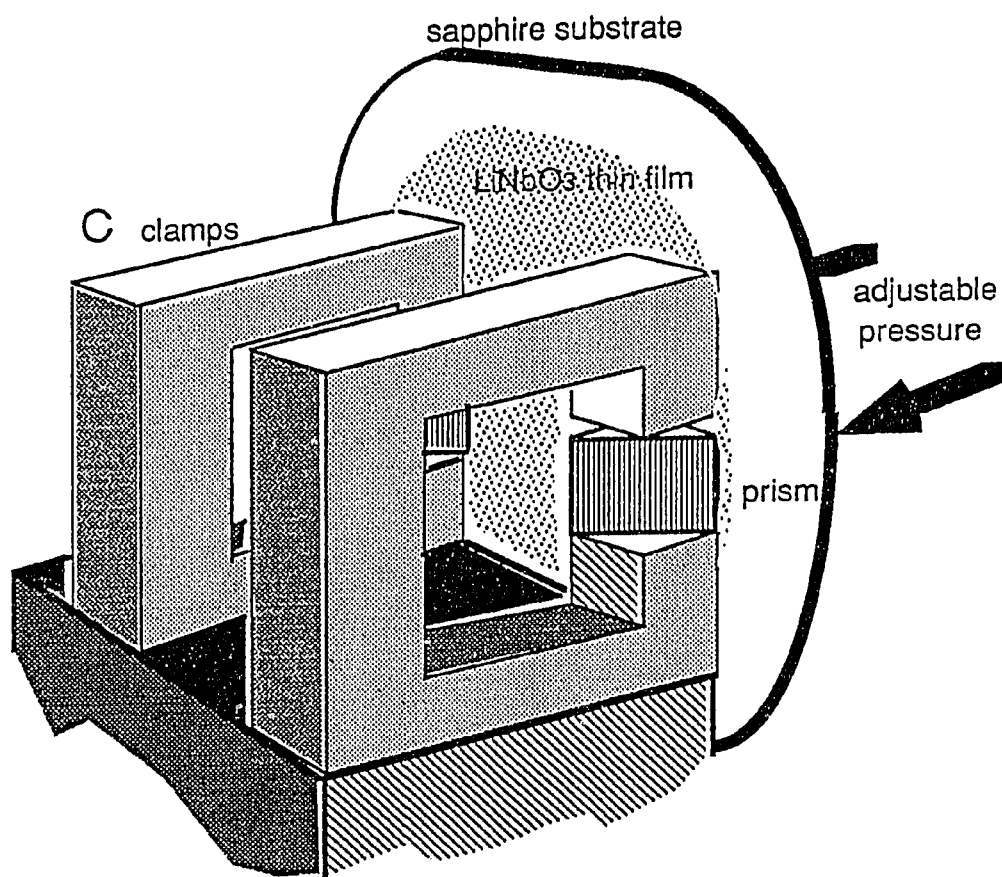


Figure 3.5 Clamping system for the prism coupler.

fore the results were not very reproducible and the prism, as well as the sample, was very susceptible to damage due to large uncontrolled pressure. With this air cylinder set-up, not only the life time of the fragile prism and sample is greatly extended, but the experimental results are very reproducible. A uniform air gap between the prism and the waveguide is then obtained and its thickness can be adjusted by varying the applied pressure.

The above described system is then installed on a turntable, which is combined with two horizontal micropositioners, with the normal to the triangular faces of the prism located very near the rotation axis of the turntable. As soon as the laser beam is incident into the prism at the proper angle, the so-called *synchronous direction*, a streak of guided light is observed. At this moment, the angle of incidence is measured and used to compute the thickness and the refractive index of the thin film. The computer program is listed in Appendix A. At least two mode angles are needed to be able to perform this calculation. If more than two modes are observed, the standard deviation is also calculated by the same program. Since the refractive index of the thin film deviates only slightly from its bulk characteristic and the thickness of the thin film can be roughly estimated from the sputtering time, another computer program has been written for computing the expected mode angles by making use of the above assumptions and other known parameters. The use of this program, which is listed in Appendix B, saves a lot of time and labor for such a manual scanning system and avoids missing any mode angle.

An output prism is sometimes used to couple the guided wave out of the thin film. It is arranged exactly the same way as the input prism, except that their vertical edges are facing each other. The distance separating the two prisms is arbitrary, but longer separation is always preferred since the longer it is, the more data we can take for determining the attenuation constant of the waveguide. The methods for measuring the attenuation constant will be discussed later.

The greatest feature of this method is that it is easy to manipulate. However, it has some disadvantages. This method depends on dust particles distributed within the air gap acting as spacers between the prism and thin film. It is obvious that the stability or reproducibility of this configuration is limited by the dust particles of random distribution and size.

In addition, the right angle of the prism needs to be a very sharp edge to prevent the guided wave from coupling out of the waveguide immediately at the spot of in-coupling and thus produce a high coupling efficiency. The prism may become unusable for such a configuration if the right angle edge is eventually crushed. Although the pressure is carefully controlled, damage to the right angle of the prism can still occur.

For correcting the problems caused by randomly distributed dust particles, an aluminum thin film was evaporated onto the surface of a 6×6 mm prism as shown in Figure 3.6. A 1.5 mm separation between the two aluminum strips is maintained to keep the evanescent field from being disturbed by the aluminum strip. The thickness of the aluminum thin film is about $1 \mu\text{m}$. This spacer produces a linearly tapered air gap which not only increases the coupling efficiency, but also eliminates the problem of random particles. The idea of such a spacer was first reported by G. L. Tangonan et al. [40]. They formed the tapered gap by placing the vertical prism edge of a rutile prism onto 5000 Å photoresist pads for a prism of 6 mm base length. The taper angle used here is in rough agreement with the expected optimum angle using Ulrich's theoretical results. The experimental result of 82 % coupling efficiency was reported by them. Although this modified two-prism coupler method does not require a very sharp vertical prism edge, the danger that the vertical prism edge may be damaged still exists. Also, when the output prism is clamped onto the waveguide, the coupling efficiency of the input prism may be changed due to the re-deformation of the waveguide. The other disadvantage of this modified two-prism is that the deformation of the sample may cause breaking of the waveguide and the substrate as well.

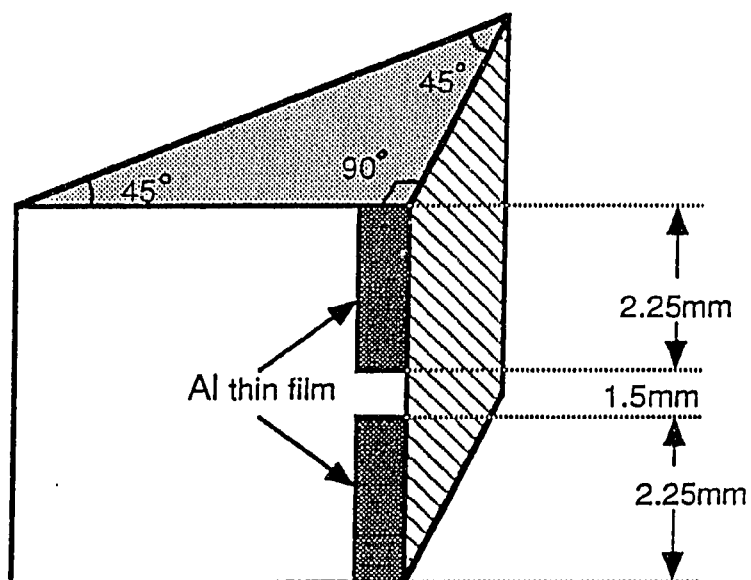
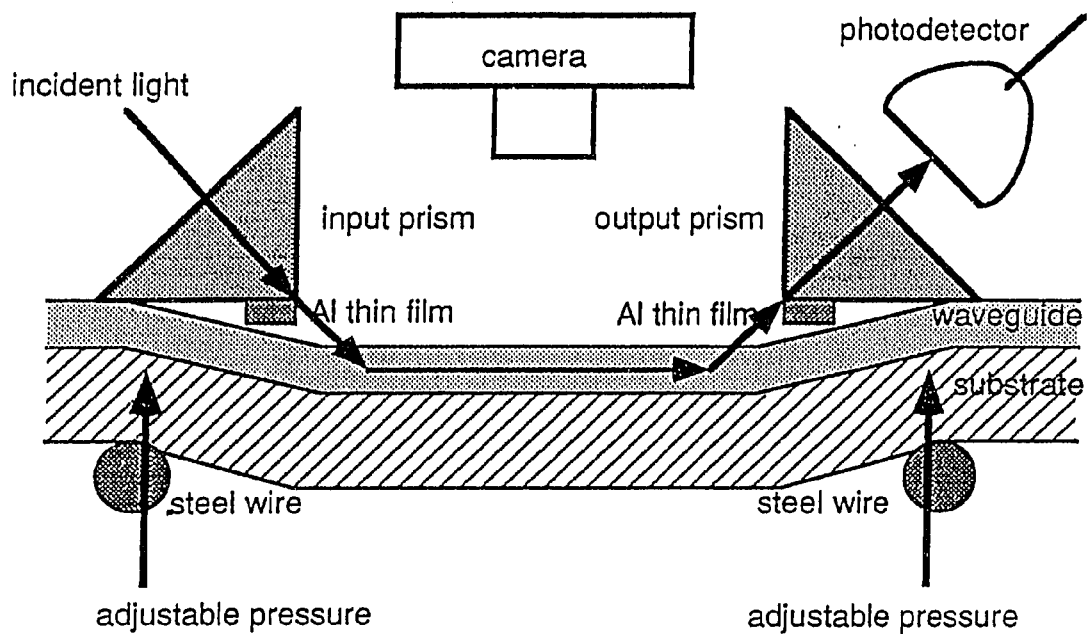


Figure 3.6 Modified two-prism waveguide coupler.

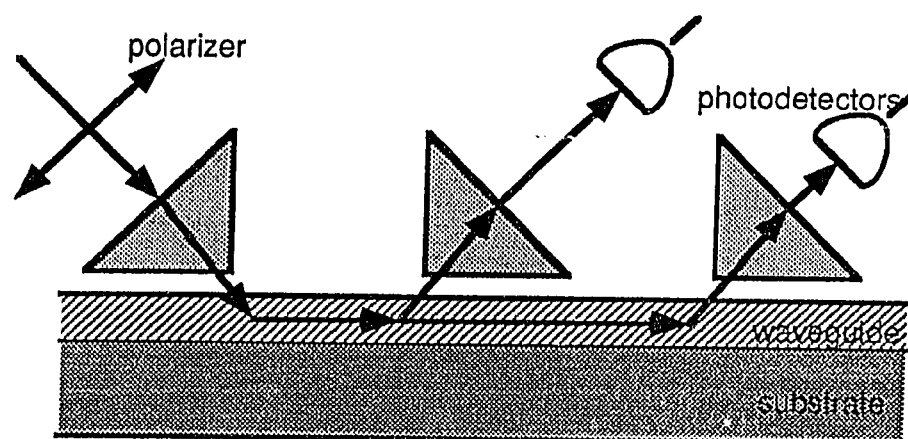


Figure 3.7 Three-prism method.

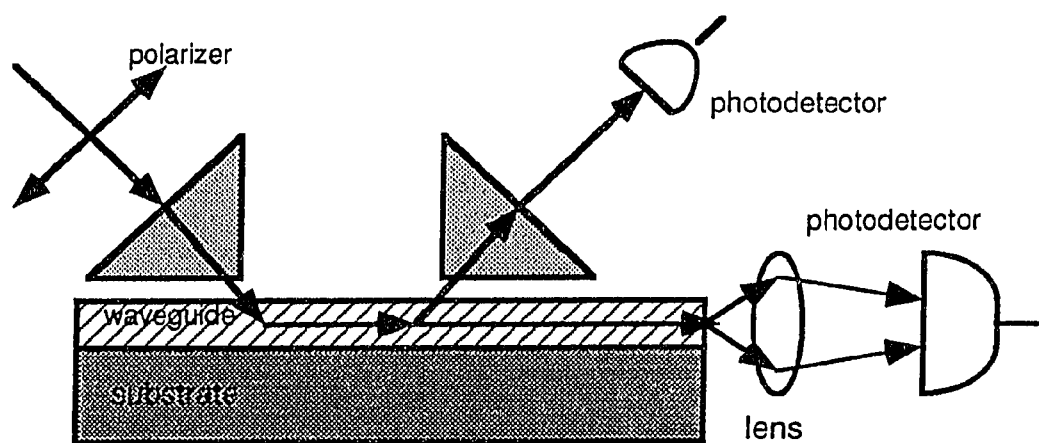


Figure 3.8 Modified three-prism waveguide coupler.

Y. H. Won et al. [45] reported a three-prism method which is claimed to be a non-destructive and highly accurate way of measuring waveguide losses. It uses three prisms, as shown in Figure 3.7, which enables the measurements to be independent of coupling efficiencies in and out of the waveguide. Since only a small strain will be required for forming a uniform air gap, it may be useful for fragile materials.

For a waveguide with high refractive index, the index of the prism is required to have a higher value for exciting the guided modes. In our case, lithium niobate has a refractive index of 2.2, and therefore the use of rutile prism ($n = 2.5$) is necessary. However, it is very expensive and this places a restriction on the three-prism method. It should be noted that this method still can not prevent the vertical prism edge from being crushed, although the chance is small.

M. J. Li et al. [48] have modified the three-prism method as shown in Figure 3.8, where the output through the third prism is replaced by end-fire coupling through the polished extremity of the waveguide. Although the three-prism method and its modification may give more accurate results, they have not yet been tried in this laboratory.

In order to reduce the number of prisms used and resolve the problem of unusable prisms with a crushed right angle, the first model of prism coupler, which was developed by P. K. Tien, R. Ulrich, and R. J. Martin [26], was reexamined. As shown in Figure 3.9, this configuration is only good for measuring refractive index and thickness of the waveguide. The streak of guided light is hardly observed since in- and out-coupling occur at the same point. D. Sarid [42,43] then proposed the other construction for the single-prism waveguide coupler shown in Figure 3.10. The air gap in this coupler model was produced and controlled by a $0.5 \mu\text{m}$ copper strip and two 0.32 cm ball bearings. The rutile prism has a base of 1×1.4 cm. A measured coupling efficiency of 94 % was reported for this configuration. A drawback of this construction is that the waveguiding length is limited by the dimension of the prism. Therefore, if a longer guiding length is required, the prism has to be propor-

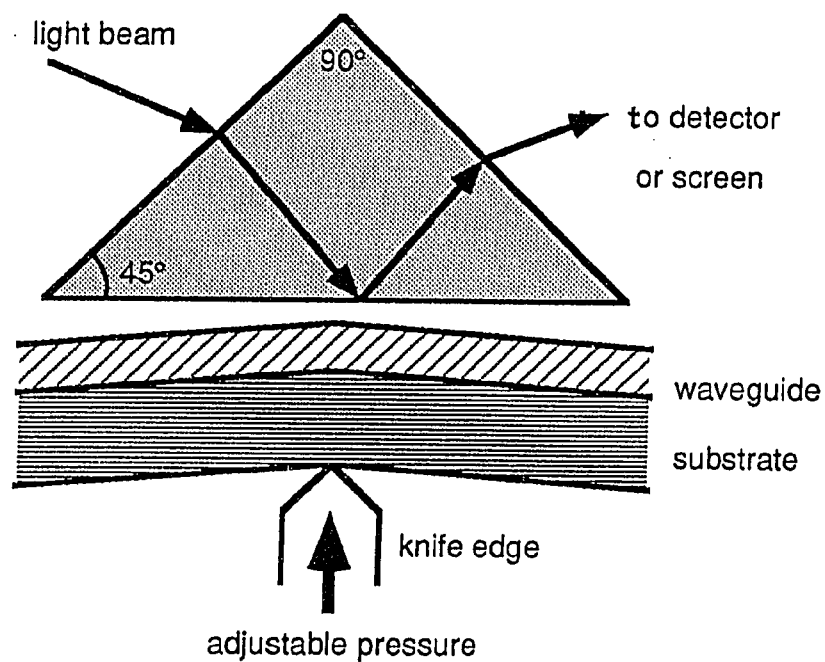


Figure 3.9 Single-prism waveguide coupler.

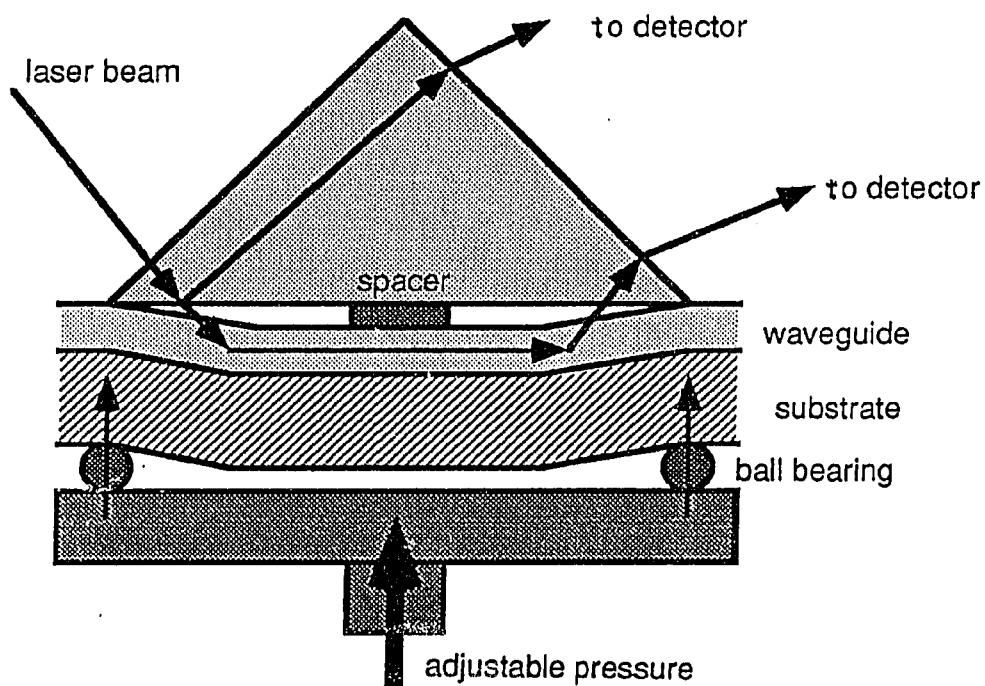


Figure 3.10 Sarid's modified single-prism waveguide coupler.

tionately larger. Because the waveguiding streak is covered by the prism, there is no way to measure the attenuation photographically. It is therefore concluded that this configuration for the prism coupler does not provide a very flexible approach.

Although the configuration modified by Sarid is not a perfect model for our needs, the same idea is used to design our own construction. As shown in Figure 3.11, a set of aluminum thin films with a thickness of $1\text{ }\mu\text{m}$ is deposited onto the base surface of the prism and a segment of steel wire is fixed on the head of the air cylinder. The theoretical profile angle predicted by Ulrich for the linearly tapered gap profile is 0.02 degree, therefore the coupling position x_c is calculated to be (1.5 mm) to the right of the steel wire, which is held at the center of the prism base. The linearly tapered air gap is expected to create a high coupling efficiency and avoid the immediate out-coupling such that the guided light can be observed outside the prism-covered region. The angle and the intensity of the reflected light can be measured, hence the thickness, the refractive index and coupling efficiency can all be determined very easily. Moreover, the attenuation constant can be evaluated photographically or photodetectively. This modified model eliminates the problems caused by the use of the vertical edge and minimizes the number of prisms used. It looks very versatile and promising, although not yet fully investigated experimentally.

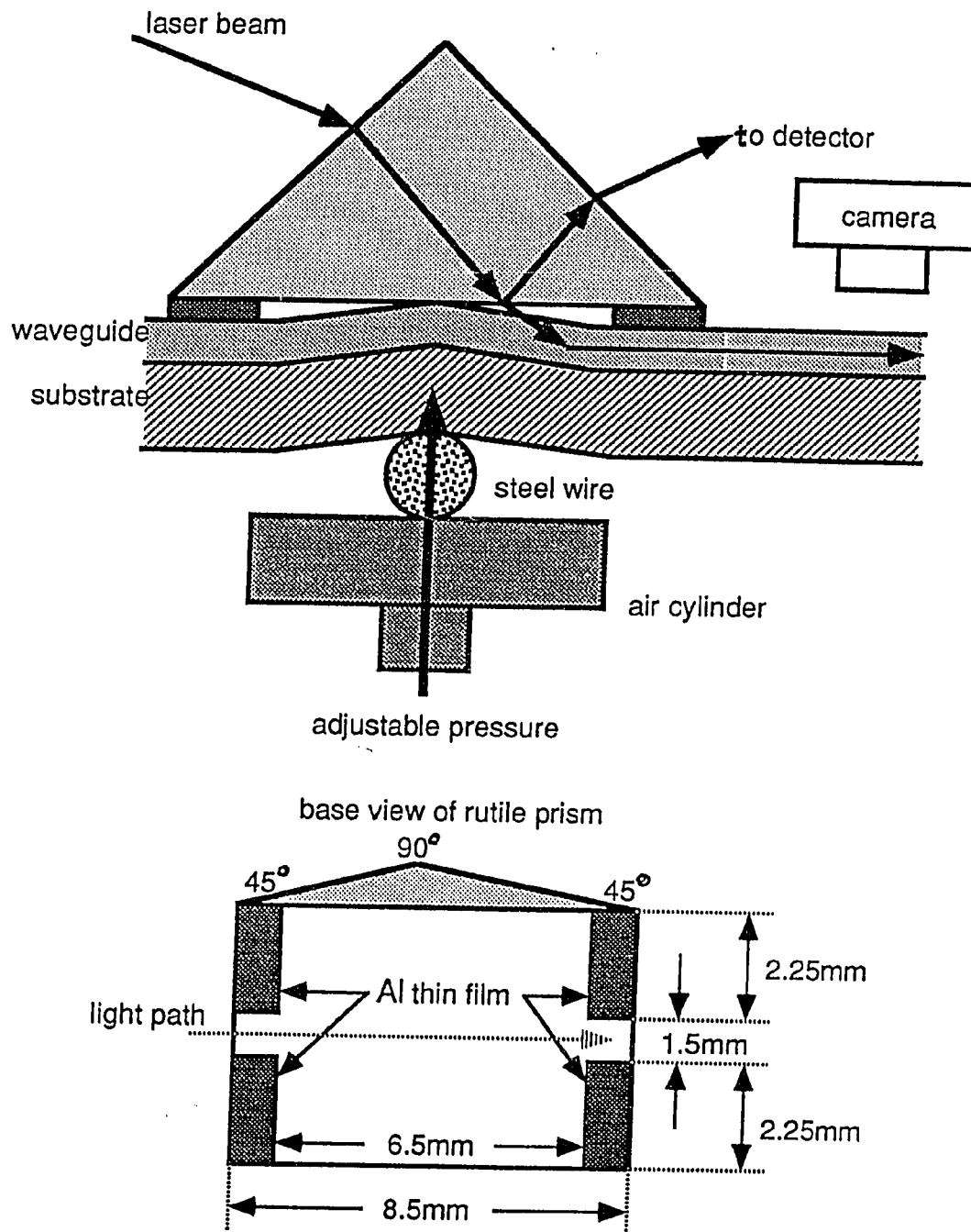


Figure 3.11 The other modified configuration

Chapter 4

Results and Discussion

4.1 Fabrication of LiNbO₃ Waveguides

In this thesis, the basic optical properties of the lithium niobate thin film waveguides rf-sputtered on sapphire substrates with different orientations were examined. Table 4.1 shows the lattice constants and ordinary and extraordinary refractive indices of LiNbO₃ and sapphire. To fabricate a high quality optical waveguide, it is very important to eliminate the scattering losses at the defects along the film-substrate interface. LiNbO₃ and sapphire are of the similar crystalline structure, which helps to reduce the effects caused by lattice constant mismatching and to form highly-oriented polycrystalline thin films. Moreover, the refractive index of LiNbO₃ is much greater than that of sapphire, which fits the requirement to form an optical waveguide and allows a wide range of fundamental wavelengths to be phase-matched.

Through an electrical discharge, the sputtering gas Ar can be made into a plasma and its positive ions then bombard the target made of powdered LiNbO₃ to produce thin films when particles are kicked out and deposited onto a substrate. Typical growth conditions of the thin film deposited by the rf diode sputtering are listed in Table 4.2. The target consisted of LiNbO₃ powder with 10% Li₂O to compensate

Crystal	Lattice type	Structure	$a_H(\text{\AA})$	$c_H(\text{\AA})$	n_o	n_e
LiNbO ₃	Rhombohedral	R3c	5.149	13.862	2.289	2.201
Sapphire	Hexagonal	R3c	4.758	12.991	1.766	1.758

Table 4.1 Some parameters of lithium niobate and sapphire at room temperature and $\lambda = 6328 \text{ \AA}$. [22]

for lithium loss which occurs during sputtering. The target was separated by 6 cm from the sapphire wafer, which was heated to 580°C during the process. The reactive sputtering atmosphere was a gas mixture of 60 % argon and 40 % oxygen at a pressure of 6 mTorr. The accumulation rate under the condition of this table is about 240 Å/hr. The LiNbO₃ thin films fabricated at such a low rate are very uniform and optically transparent. X-ray diffraction (XRD) has been used to analyze the crystallinity of the films.

4.2 Crystallinity of Thin-Film LiNbO₃

X-ray diffraction (XRD) has been used to examine the crystallinity of the sputtered films. The x-ray diffractometer consists of a Phillips Electronics Type 12045/3 x-ray generator fitted with a copper x-ray tube, a x-ray detector, and a x-ray goniometer equipped with a stepper motor. A computer was used to control the x-ray diffractometer and to analyze the detected data. A voltage of 35 kV and a current of 20 mA were used to excite radiation from the x-ray tube. A nickel filter was placed to absorb copper K_β radiation and thus create a nearly monochromatic Cu K_α radiation with a wavelength of 1.5418 Å. The pulse height analyzer baseline voltage was set to 1.0 V to reduce electronic noise.

Target	LiNbO ₃ + 10 % Li ₂ O
Substrate	Al ₂ O ₃
Separation	6 cm
Pressure	6 mTorr
Temperature	580°C
Gas ratio	60% Ar + 40% O ₂
Pre-sput. time	25 min
Rf power	150 W

Table 4.2 Sputtering conditions in the present experiment.

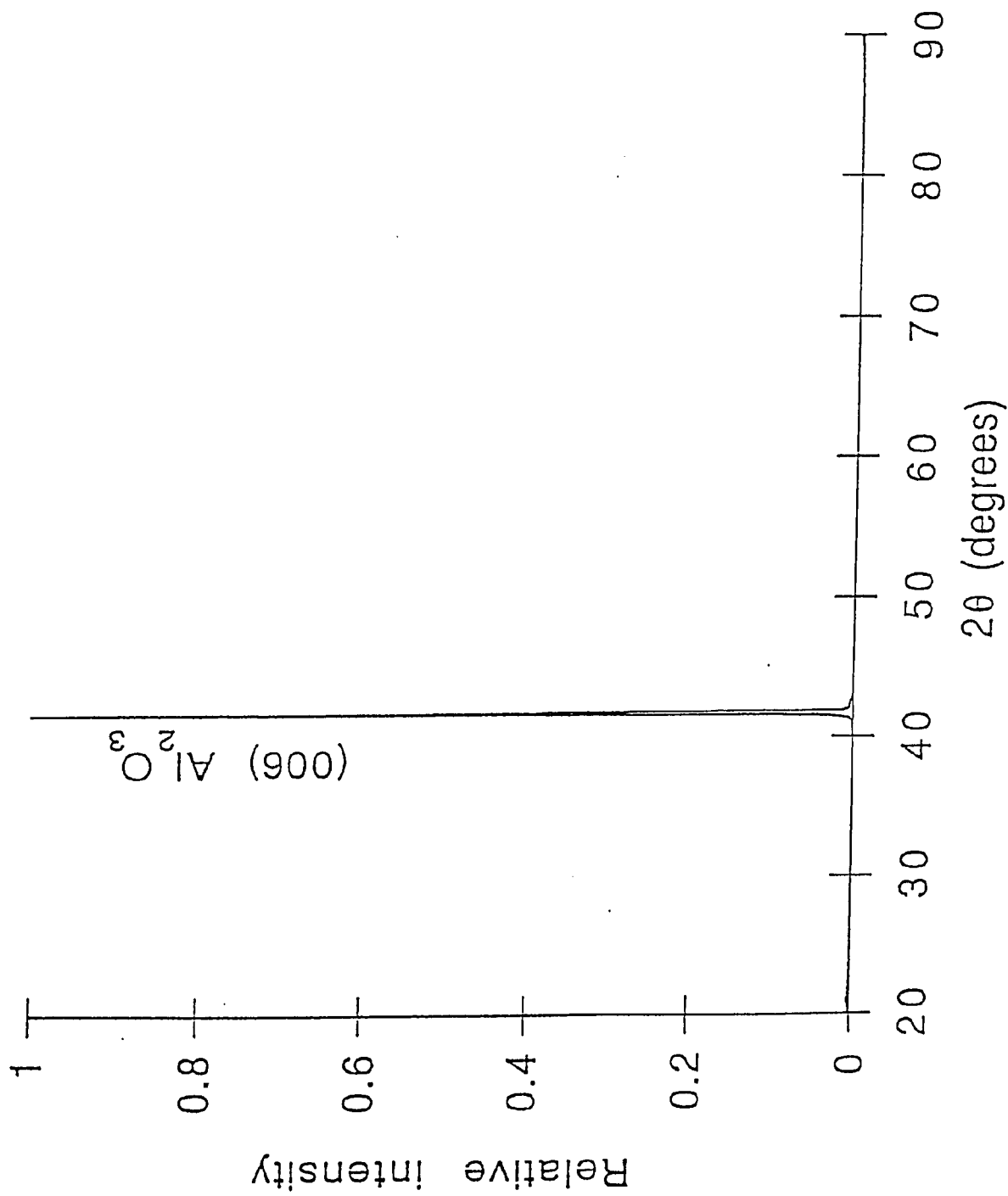


Figure 4.1 XRD pattern of (001) sapphire substrate.

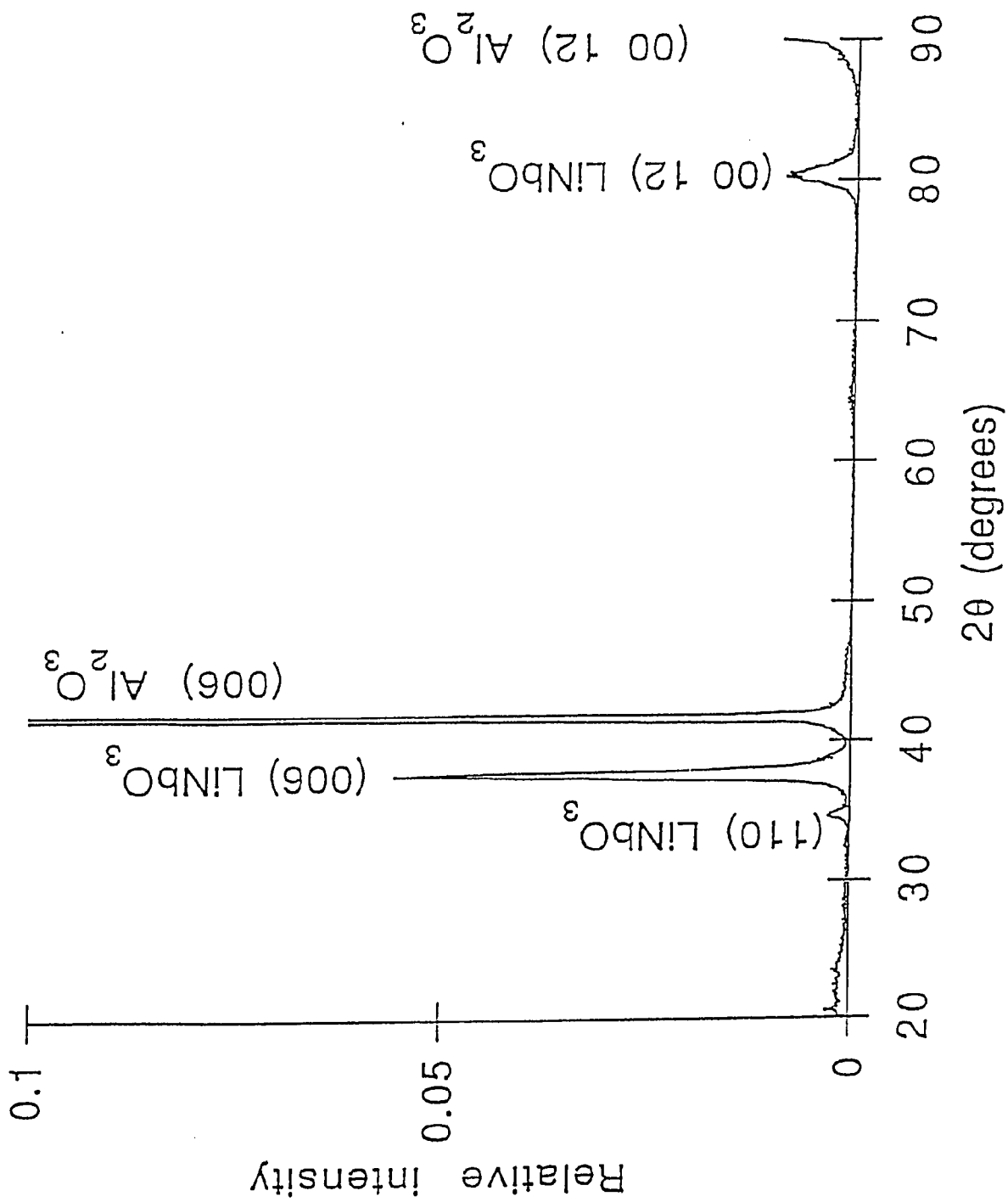


Figure 4.2 XRD pattern of LiNbO_3 film on (001) sapphire.

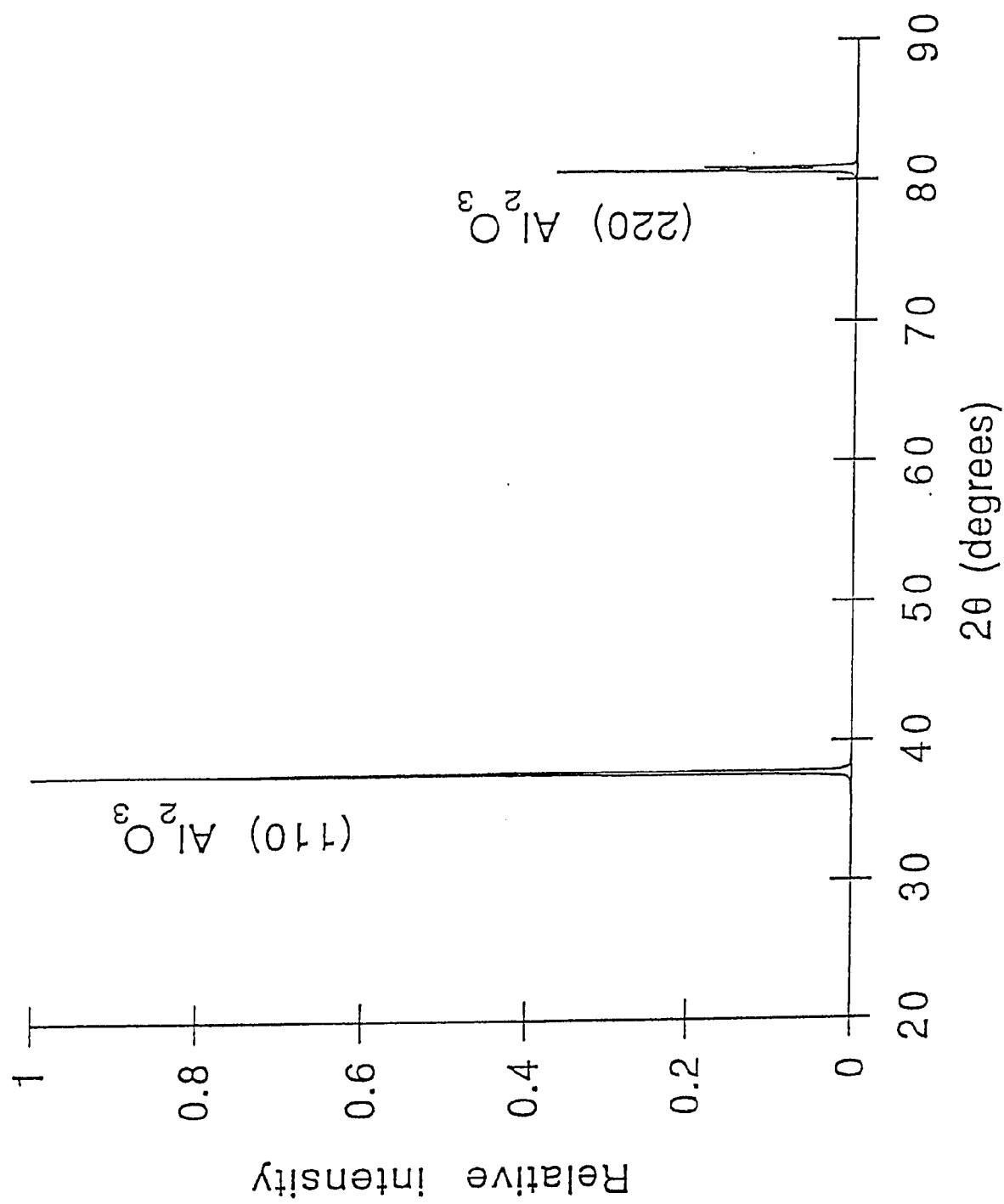


Figure 4.3 XRD pattern of (110) sapphire substrate.

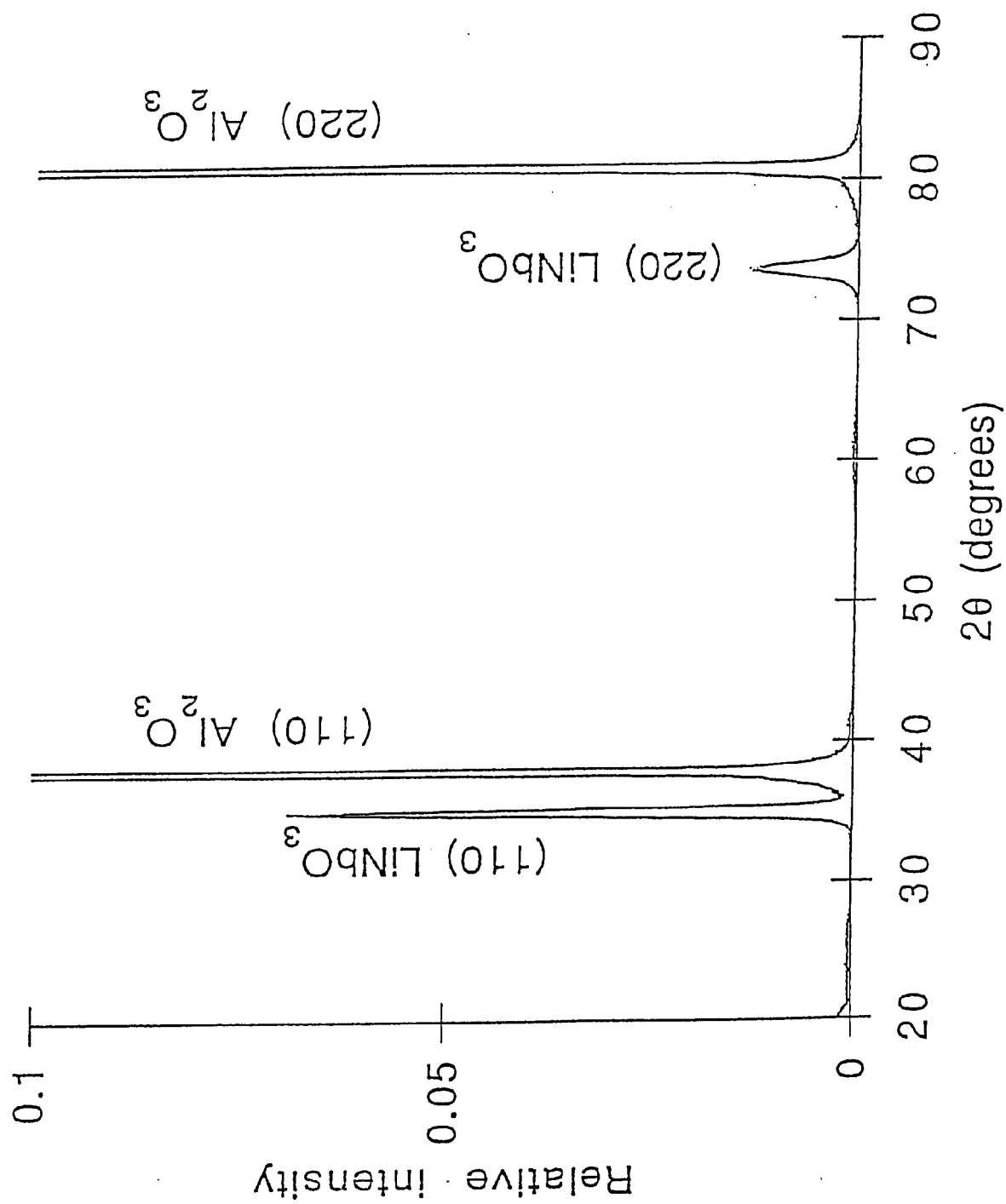


Figure 4.4 XRD pattern of LiNbO_3 film on (110) sapphire.

Single crystal sapphire substrates with (001) and (110) orientations were used in this study. X-ray scans were taken for lithium niobate thin films on sapphire substrates as well as for blank substrates. The angles scanned were from $2\theta=20^\circ$ to $2\theta=90^\circ$ with 0.02° steps and a dwell time of 1.0 second at each step. One can see in Figures 4.2 through 4.4 that the as-sputtered lithium niobate thin films are highly oriented polycrystalline with the c axis parallel to that of the substrates. The XRD peaks are listed in Table 4.3. Note that the (006) peak is shifted 1.33° off the powder diffraction value and the lattice constant c_H of lithium niobate on (001) sapphire was calculated to be 14.334 \AA , which is greater than the bulk value of 13.862 \AA . Since the unit cells of lithium niobate tend to maintain the same volume as its bulk material, the shrinkage of the lithium niobate lattice constant a_H near the film-substrate interface causes the expansion of its lattice constant c_H . Also, there is a very small peak, as shown in Figure 4.1, located on the high side of the shoulder of the (006) peak and at the position of 38.88° , which is close to the powder diffraction value. The fine structure of the (006) peak pattern indicates that the lattice constant mismatch of the two a_H 's (about 7.59 %) at the film-substrate interface causes the shrinkage of a_H and the expansion of c_H of lithium niobate, as shown in Figure 4.5, while the distortion effect is greatly reduced as more and more lithium niobate layers are built up. This effect was not observed on the (110) sample since the mismatch of the two c_H 's is smaller and has a value of about 6.28 %. The width of the lithium niobate peaks was calculated to be about two to three times that of the single crystal sapphire. The broadening is primarily due to the polycrystallinity and the thickness of the thin film.

In addition to XRD, the observation of birefringence is another way to determine the crystallinity of thin films made with an anisotropic material.

Sapphire	2θ	Width	Description	Lattice constant
(001)	34.72°	0.30°	(110) LiNbO_3	$c_H = 14.334 \text{ \AA}$
	37.64°	0.53°	(006) LiNbO_3	
	41.68°	0.18°	(001) Al_2O_3	
(110)	34.88°	0.49°	(110) LiNbO_3	$a_H = 5.144 \text{ \AA}$
	37.76°	0.20°	(110) Al_2O_3	

Table 4.3 X-ray diffraction data.

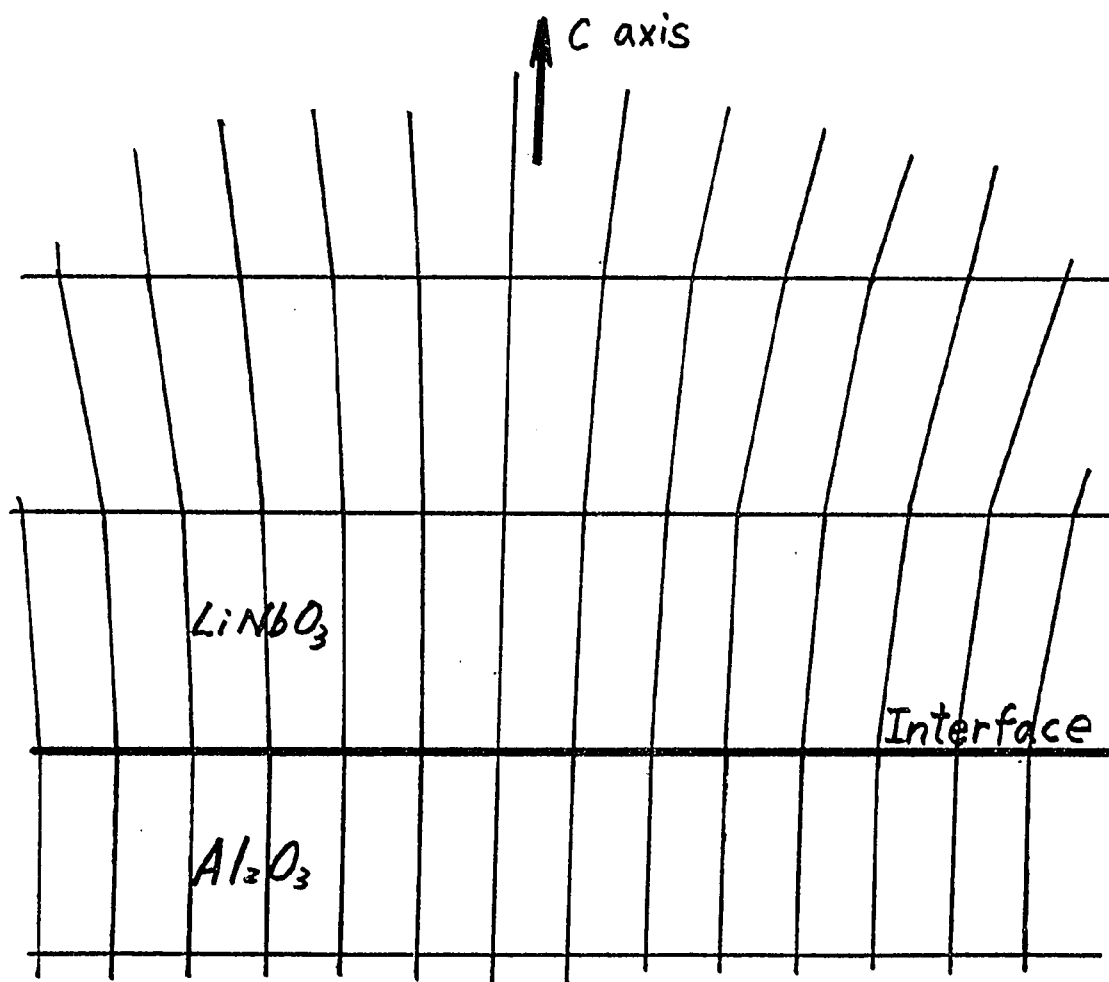


Figure 4.5 Distortion of the lithium niobate unit cells near the interface due to lattice mismatch.

4.3 Measurement of Refractive Index and Thickness

Since the modified single-prism coupler shown schematically in Figure 3.11 has not yet been completely constructed, the original configuration shown in Figure 3.9 was implemented to measure refractive indices and thicknesses of the waveguides. A polarized He-Ne laser beam with a wavelength of 6328 Å was coupled into the LiNbO₃ waveguide by a 45°-45°-90° rutile prism. The output of the laser was detected after reflection through the same prism by measuring the current from a silicon photosensor. The rutile prism was mounted on a turntable equipped with an x-y micropositioner. The angles between the laser beam and the normal to the prism face were read from the turntable to a precision of ± 1 minute of arc. The rutile prism was held by a "C" clamp shown schematically in Figure 3.5. The sample was pushed against the prism by an air-controlled piston. The pressure was adjusted by a pressure-regulator. A pressure of 15 psi was applied to the sample throughout the measurement. Measurements were made by loading the sample against the prism and rotating the turntable until coupling occurred as shown by a minimum in the power meter. The angle was recorded and the rotation continued until all the modes that the present system could couple into the film were found.

By properly choosing the incident angle, the phase matching condition can be achieved and therefore the propagation constant of the incident light can be made equal to that of the mode in the waveguide. The equation relating the incident angle and the propagation constant is given by

$$\delta = \sin^{-1} \left[\frac{n_p}{n_c} \sin \left(\sin^{-1} \left(\frac{\beta}{k_0 n_p} \right) - \alpha_c \right) \right], \quad (4.1)$$

where δ is the incident angle with respect to the normal to the input face of the prism, n_p and n_c are the refractive indices of the prism and the cover (air), respectively, β is the propagation constant in the waveguide, k_0 is the magnitude of the wave vector

propagating in air, and α_c , shown in Figure 3.1, is the corner angle of the prism. Since n_p, n_a , and α_c are already known and δ can be measured, the propagation constant can then be calculated by equations 2.15 and 2.16. If two or more modes are observed, the thickness t and the refractive index n_f can be evaluated by these mode condition equations. Typically, for a lithium niobate waveguide with a thickness of about $0.6 \mu\text{m}$, three modes can be observed for both TE and TM waves. However, the angle of the TM_0 mode was sometimes too large to be observed by our set-up due to the physical restriction of the fixed prism angles. In this case, a prism with a different corner angle α_c has to be implemented instead of the one previously used. The measured angles were then used to calculate the refractive indices and the thickness of the waveguide. The plots of the reflected intensity vs. incident angle (δ) are shown in Figures 4.6 through 4.11, in which the bottoms of the dips correspond to the mode angles. Since the intensity of the light reflected at the input face of the prism increases while the angle of incidence (δ) increases, the intensity of the reflected light detected at the output stage thus decays with increasing incident angle. This effect causes the dips to be shifted by an amount of approximately a $+0.2^\circ$. If one neglects the dips of the curves, the curves look like straight lines monotonically decreasing with increasing angle of incidence. Correction to the angular shift can be made by subtracting the measured data from the corresponding straight line, which yields another curve similar to the one shown in Figure 4.12. The dips now become peaks, and the position of the individual peak center can be located by the three-point fitting method suggested by Koistinen and Marburger [57], as shown in Figure 4.13. The center point of the three chosen data points should be the closest one to the maximum of the peak. The other two points must have about 85 % intensity of the maximum and be separated by two equal intervals from the center point. The center of the peak is given by

$$h = x_1 + \frac{c}{2} \left(\frac{3a + b}{a + b} \right), \quad (4.2)$$

where $a = y_2 - y_1$, $b = y_2 - y_3$, and $c = x_2 - x_1 = x_3 - x_2$. The location of the peak can be determined to within 0.02° .

The thickness and refractive indices corresponding to different modes of the LiNbO_3 thin film are tabulated in Table 4.4. The data measured from the sample on (110) sapphire are chosen to serve the sample calculation here. The measured mode angles are

$$\delta_{TE2} = -6^\circ 56' \pm 1' = -6.93^\circ \pm 0.02^\circ,$$

$$\delta_{TE1} = 9^\circ 01' \pm 1' = 9.02^\circ \pm 0.02^\circ,$$

$$\text{and } \delta_{TE0} = 19^\circ 05' \pm 1' = 19.88^\circ \pm 0.02^\circ.$$

After correcting the shifting effect due to the tilted slope, the mode angles become

$$\delta_{TE2} = -7.08^\circ \pm 0.04^\circ,$$

$$\delta_{TE1} = 8.82^\circ \pm 0.04^\circ,$$

$$\text{and } \delta_{TE0} = 19.70^\circ \pm 0.04^\circ.$$

Insert the angles into Eq. 4.1 individually, we obtain the propagation constants N_m corresponding to the m -th order mode,

$$n_{TE2} = 1.940 \pm 0.001,$$

$$n_{TE1} = 2.135 \pm 0.001,$$

$$\text{and } n_{TE0} = 2.251 \pm 0.001.$$

Now, we can choose any two propagation constants and then solve Eq. 2.15 for thickness t and refractive index n_f . Finally, we have

$$n_f = 2.286 \pm 0.002 \text{ and } t = 0.643 \pm 0.001 \mu\text{m}.$$

According to Table 4.4, since two different values of refractive index corresponding to TE and TM waves have been observed in each sample and the index difference is larger than the allowed error, the thin films grown by the rf sputtering method under the conditions listed in Table 4.2 exhibit birefringence and thus are polycrystalline. If the orientation of the c axis of the LiNbO_3 crystal and the propagation direction of the light in the film are known, one can then determine whether ordinary or

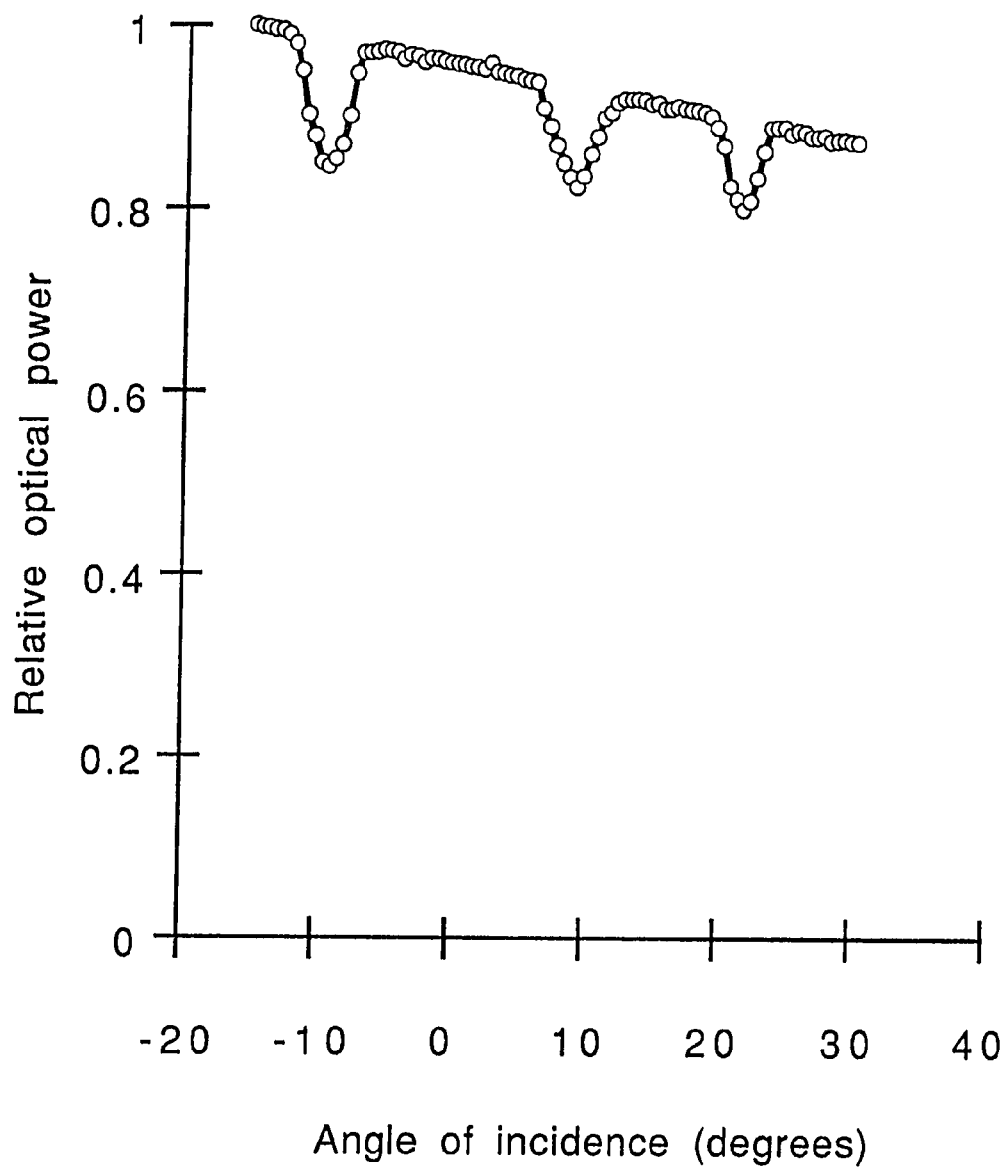


Figure 4.6 Relative intensity of reflected light vs. angle of incidence. TE modes for lithium niobate on (012) sapphire.

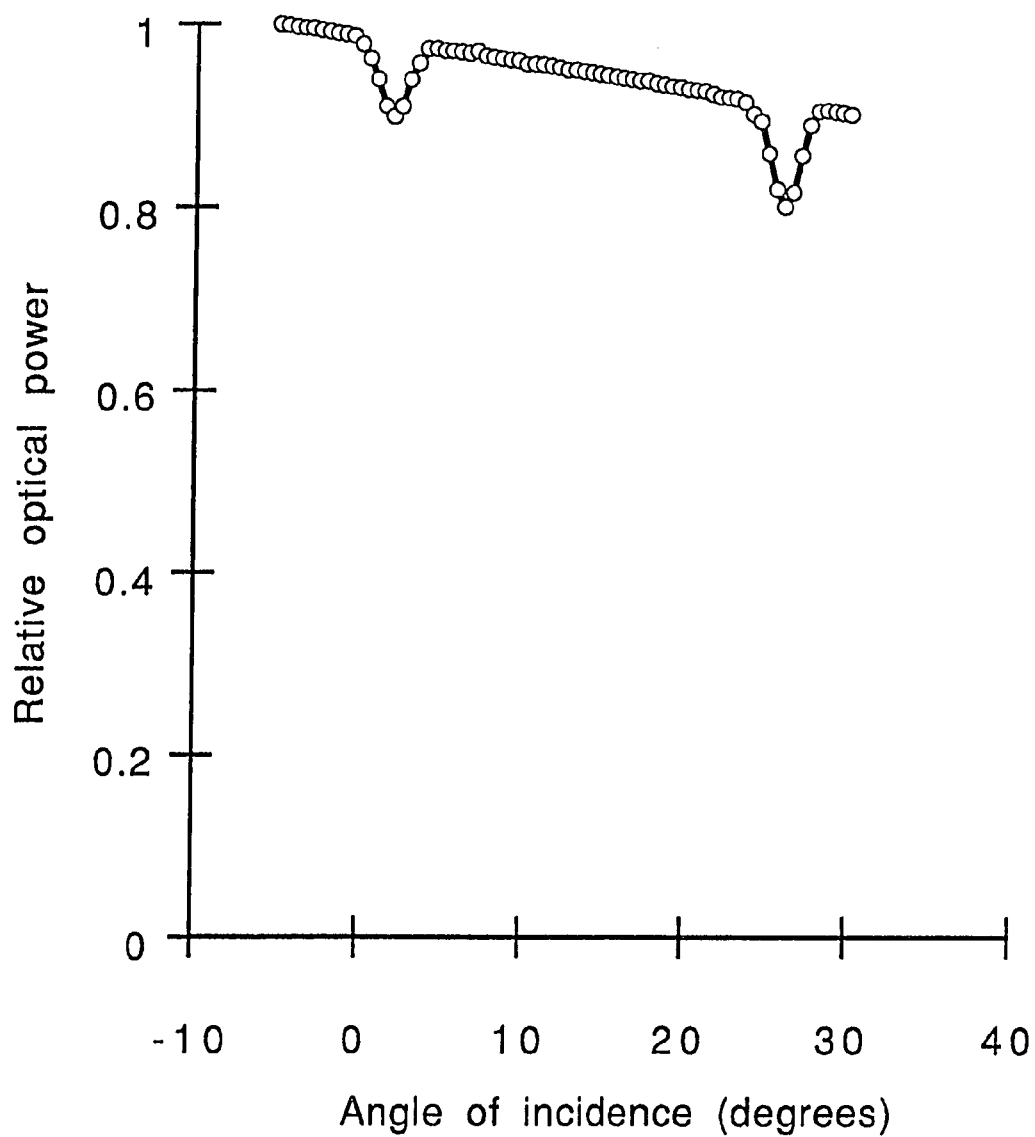


Figure 4.7 Relative intensity of reflected light vs. angle of incidence. TM modes for lithium niobate on (012) sapphire.

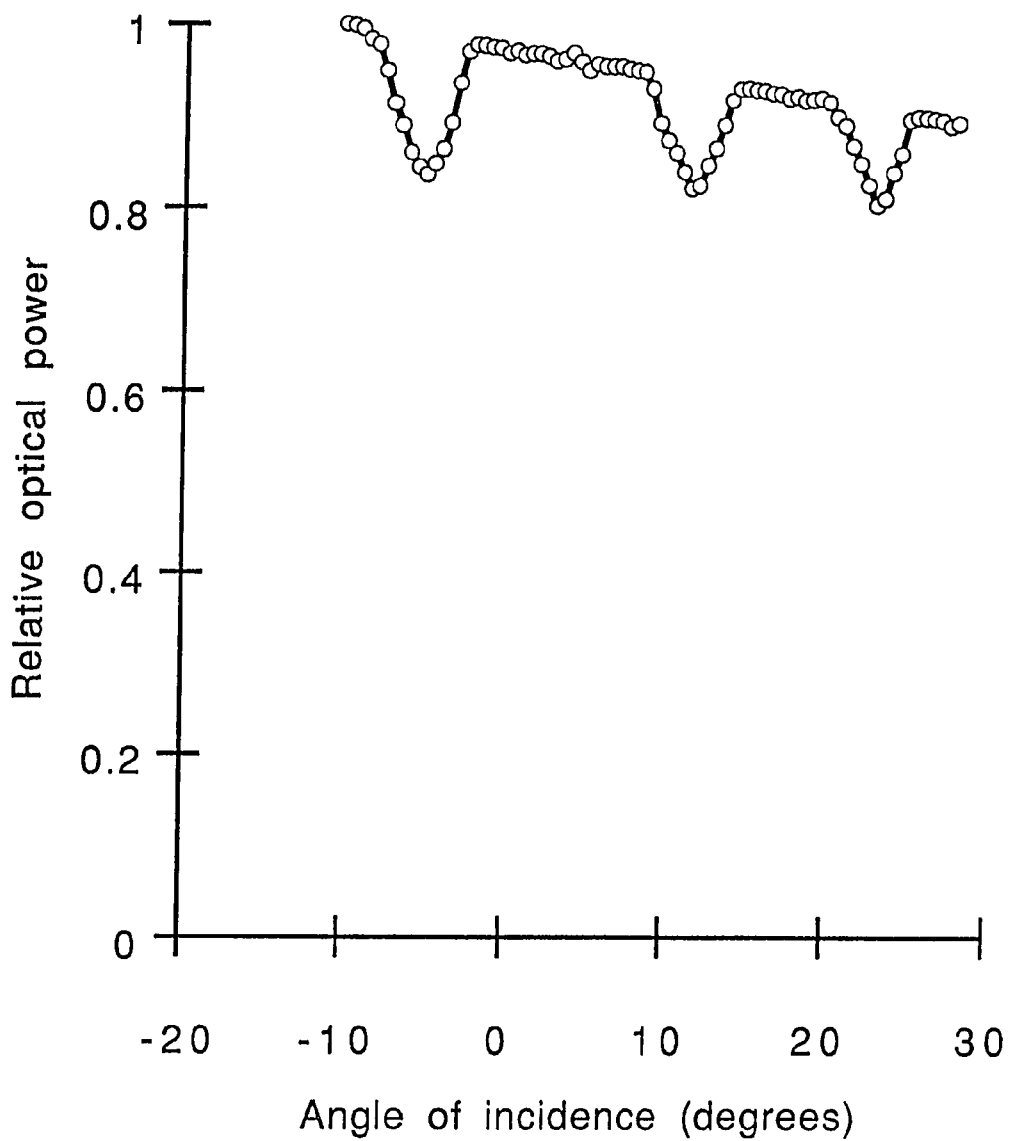


Figure 4.8 Relative intensity of reflected light vs. angle of incidence. TE modes for lithium niobate on (001) sapphire.

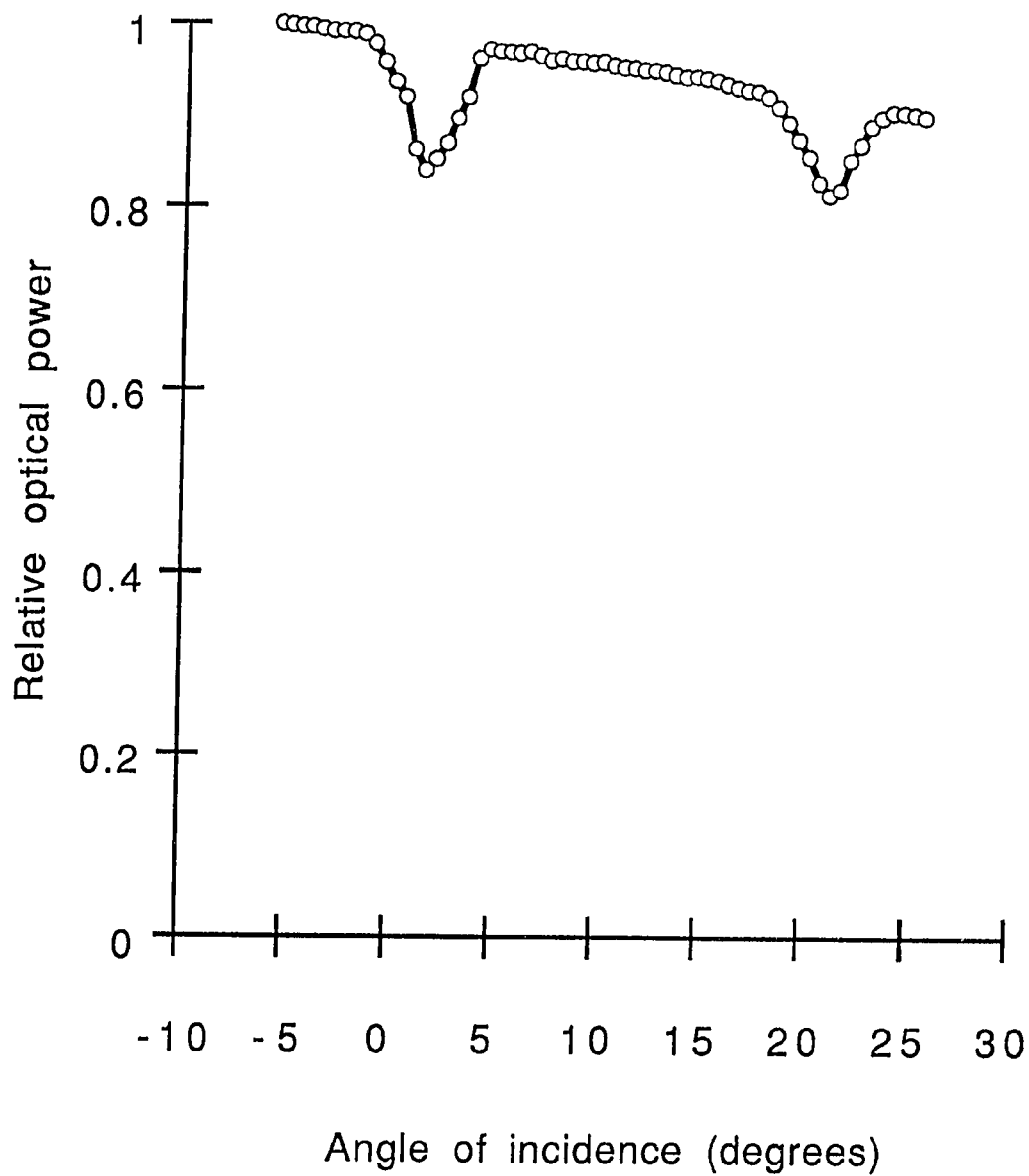


Figure 4.9 Relative intensity of reflected light vs. angle of incidence. TM modes for lithium niobate on (001) sapphire.

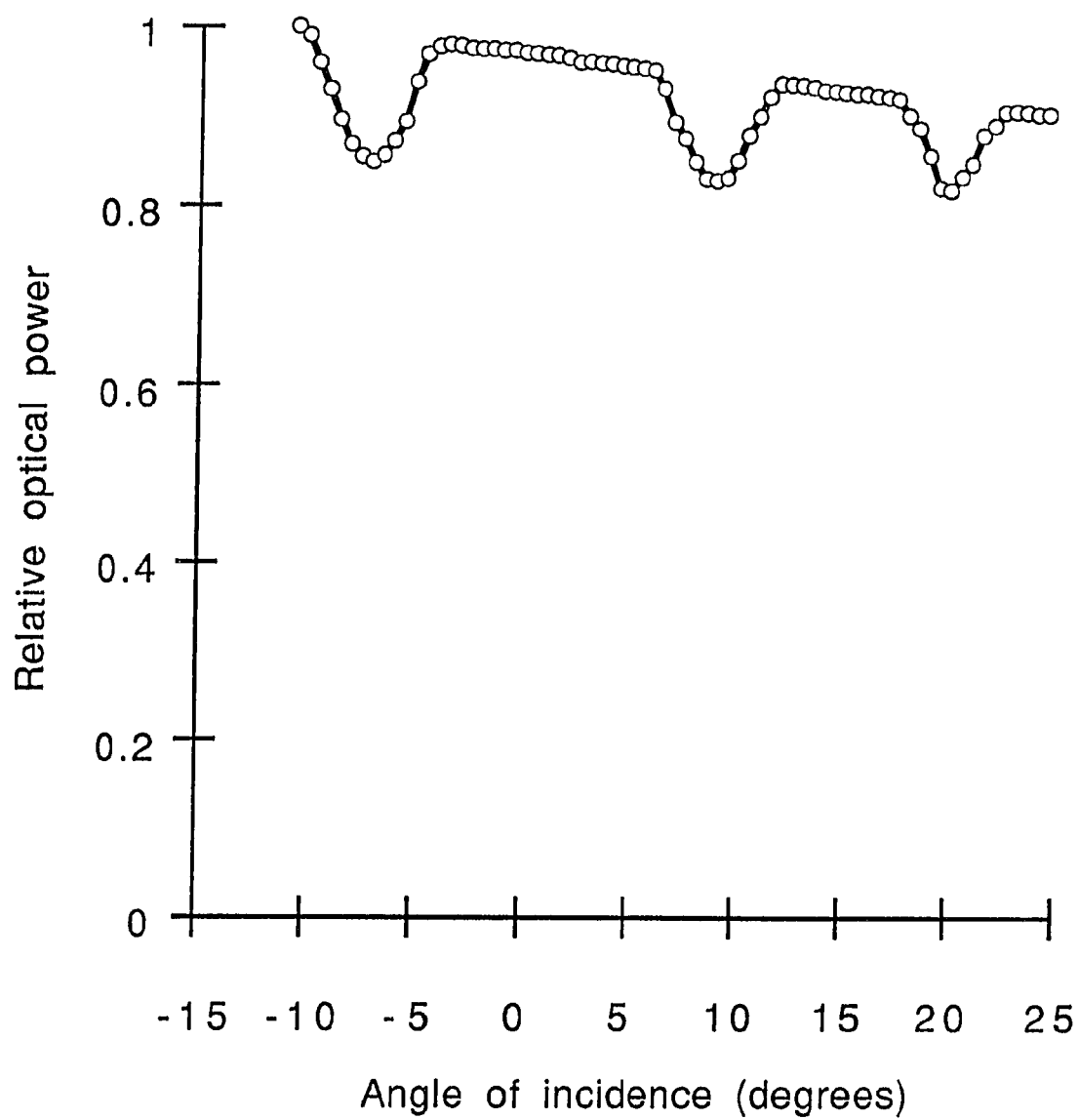


Figure 4.10 Relative intensity of reflected light vs. angle of incidence. TE modes for lithium niobate on (110) sapphire.

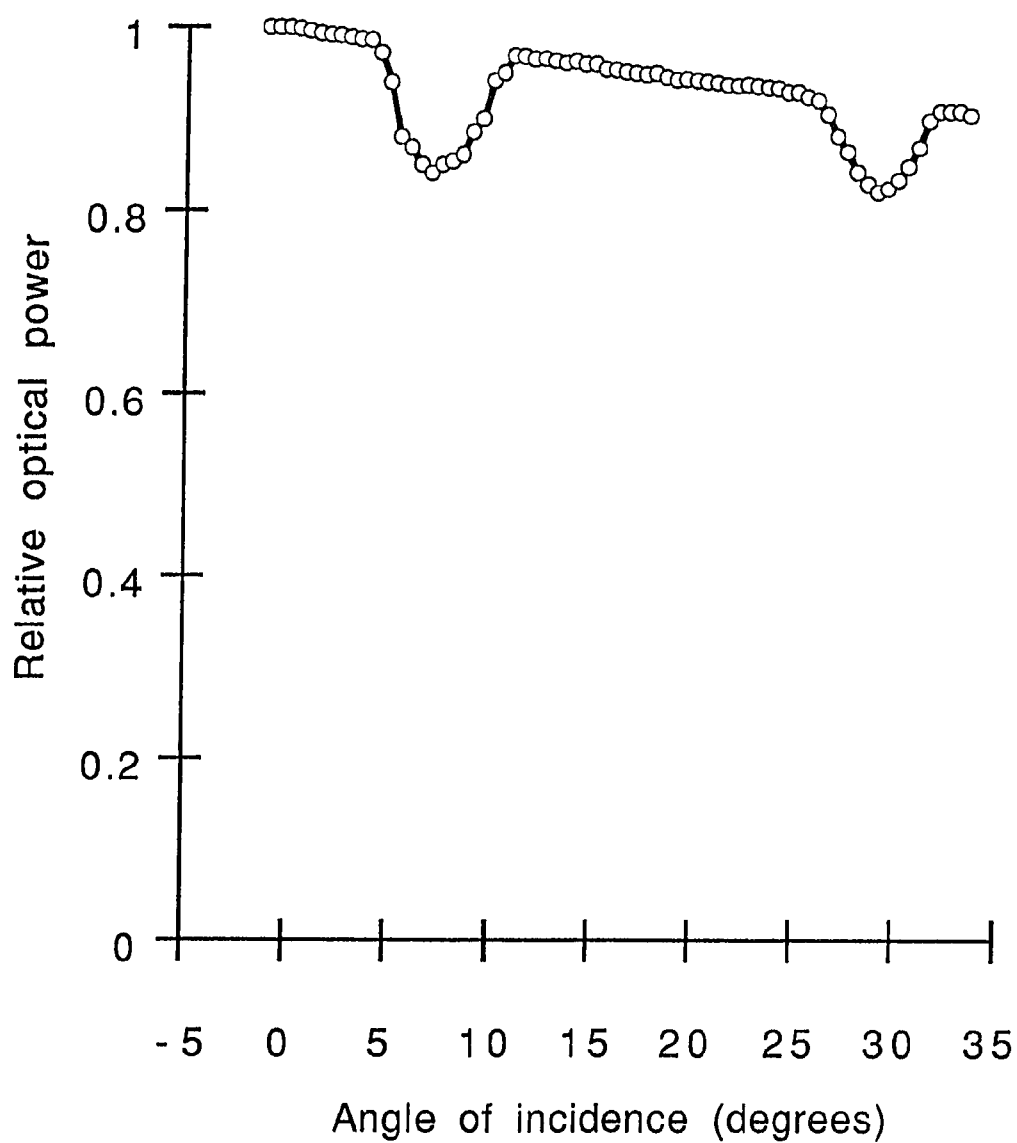


Figure 4.11 Relative intensity of reflected light vs. angle of incidence. TM modes for lithium niobate on (110) sapphire.

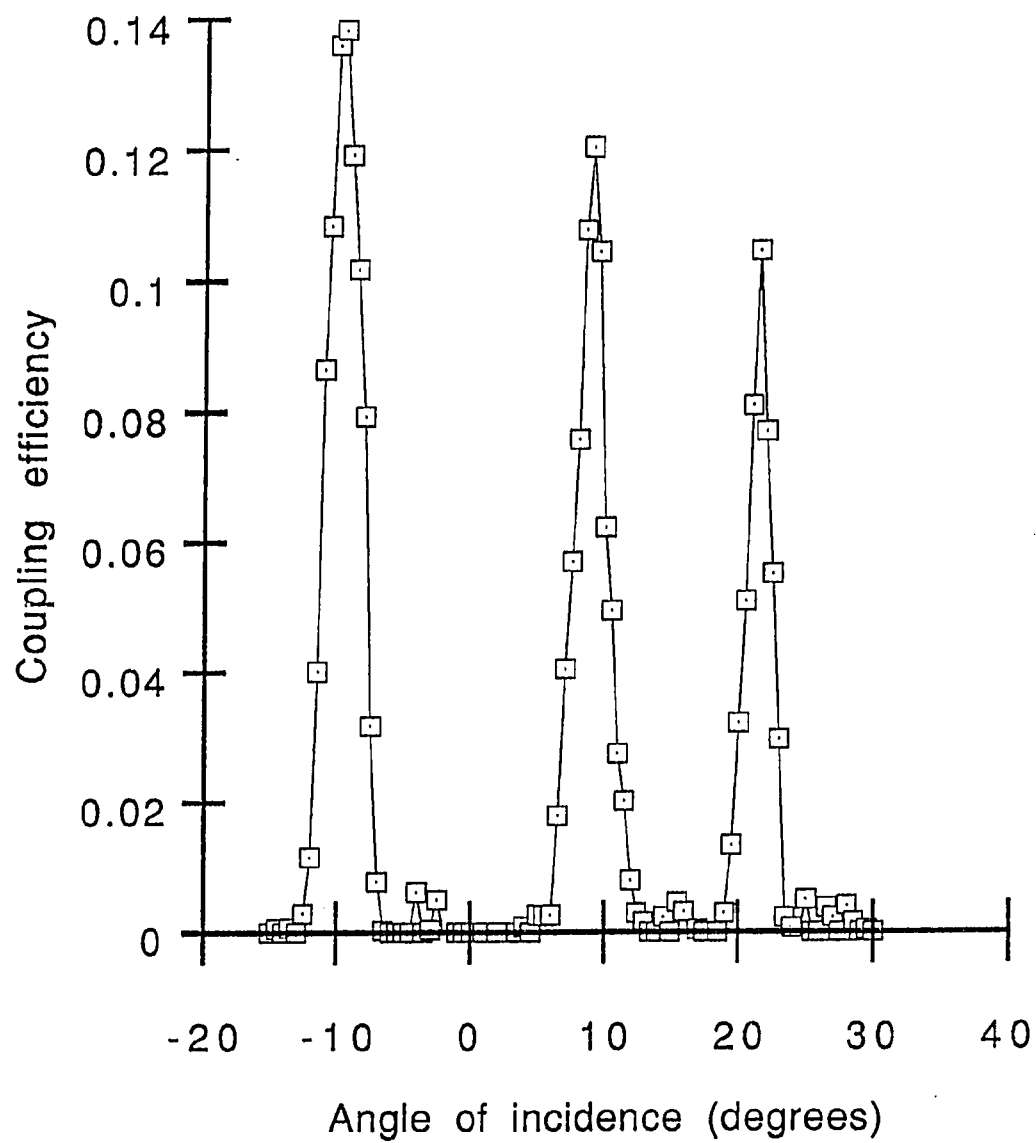


Figure 4.12 Optical power coupled into waveguide vs. angle of incidence.

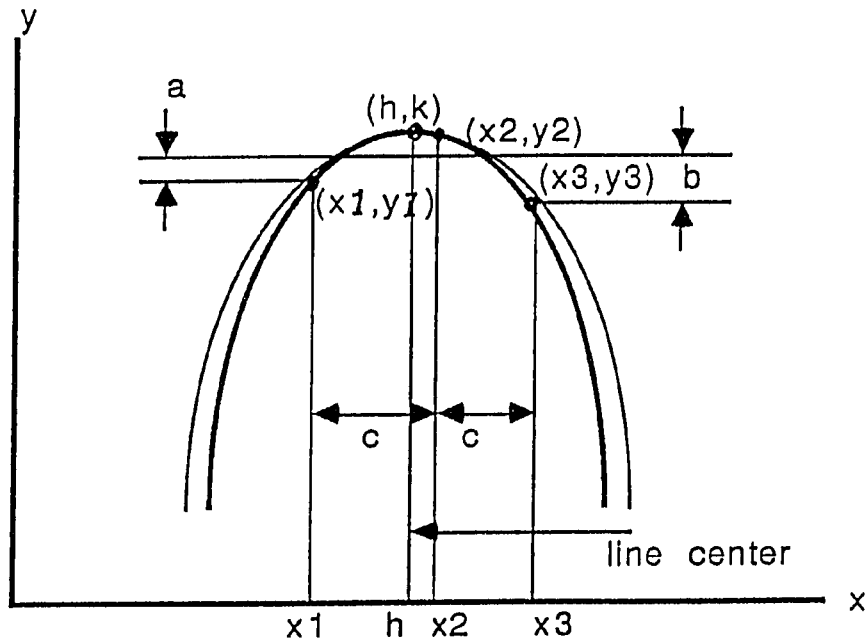


Figure 4.13 Three-point parabola fitting method.

Sapphire	Sput. time	Mode angle ($\pm 0.04^\circ$)	$n_f(\pm 0.002)$ and $t(\pm 0.001\mu m)$
(012)	24 hr	$\delta_{TE2} = -9.61^\circ$	$n_{TE} = 2.312$
		$\delta_{TE1} = 9.02^\circ$	
		$\delta_{TE0} = 21.47^\circ$	$t = 0.588\mu m$
		$\delta_{TM2} = 1.98^\circ$	$n_{TM} = 2.330$
(001)	26 hr	$\delta_{TM1} = 26.44^\circ$	$t = 0.589\mu m$
		$\delta_{TE2} = -5.03^\circ$	$n_{TE} = n_o = 2.322$
		$\delta_{TE1} = 11.57^\circ$	
		$\delta_{TE0} = 23.13^\circ$	$t = 0.631\mu m$
(110)	26 hr	$\delta_{TM2} = 1.44^\circ$	$n_{TM} = n_e = 2.263$
		$\delta_{TM1} = 22.16^\circ$	$t = 0.633\mu m$
		$\delta_{TE2} = -7.08^\circ$	$n_{TE} = 2.287$
		$\delta_{TE1} = 8.82^\circ$	
(110)	26 hr	$\delta_{TE0} = 19.70^\circ$	$t = 0.641\mu m$
		$\delta_{TM2} = 6.87^\circ$	$n_{TM} = 2.319$
		$\delta_{TM1} = 29.02^\circ$	$t = 0.648\mu m$

Table 4.4 Effective thicknesses and refractive indices corresponding to guided modes in the lithium niobate thin films deposited on sapphire.

extraordinary or hybrid ray is propagating in the waveguide [63]. For LiNbO_3 films on (001) sapphire, the c axis of sapphire is oriented normal to the plane of the substrate, and so is that of the film. We can thus relate n_{TM} and n_{TE} to n_e and n_o , respectively, such that $n_o = n_{TE} = 2.322$ and $n_e = n_{TM} = 2.263$ at $\lambda = 6328\mu\text{m}$. The index difference of the two measured values is 0.059, which is less than that of the bulk values (0.088). For the sample on (110) sapphire substrate, the c axis of the film was determined to be in the plane of the substrate. However, the c axis of the film could be in any direction with respect to the c axis of the sapphire substrate. Hence, it is necessary to rotate the wafer with respect to its normal and then measure the refractive indices of the film. The maximum and minimum values should occur in the same measurement and they correspond to the ordinary and extraordinary refractive indices of the film, respectively. The indices for the film on the (110) sapphire substrate were determined to be 2.319 and 2.287 for n_{TM} and n_{TE} , respectively. The difference 0.032 is even smaller than that of the (001) sample, which implies that the propagation direction of the guided wave was neither parallel nor perpendicular to the c axis of the film and both ordinary and extraordinary rays were guided in the waveguide. In order to exactly relate the index of TE or TM mode to the index of the ordinary or extraordinary ray, the knowledge to the relationship between the propagation direction of the light and the orientation of the c axis of the film is required. Further effort will be placed on solving this problem in future research.

The calculated effective thicknesses were then used to determine the deposition rate of the rf sputtering under the conditions described above. The deposition rate was estimated to be about $240\text{\AA}/\text{hr}$. Lithium niobate films with thicknesses less than $0.1\mu\text{m}$ are usually too thin to support a TM guided mode so that measurements with a prism coupler are not possible. Table 4.4 shows the cutoff thicknesses corresponding to different modes, which were calculated by equation (11.2-14) in Reference 10. If the thickness of the waveguide is less than its cutoff value of the zeroth order mode,

Mode	Thickness (λ)	Thickness (\AA) ($\lambda=6328\text{\AA}$)
TE0	0.085 λ	537 \AA
TE1	0.426 λ	2692 \AA
TE2	0.766 λ	4848 \AA
TM0	0.150 λ	949 \AA
TM1	0.491 λ	3104 \AA
TM2	0.831 λ	5260 \AA

Table 4.5 Cutoff thicknesses corresponding to different modes. $n_f=2.2$ and $n_s=1.77$.

then no mode can be supported by the waveguide. The thickness restriction is a limitation of the measurement by the coupling technique.

From the reflected intensity plots, the coupling efficiency was estimated to be lower than 20 %. Although high coupling efficiency is not the main concern in this study, it is believed that much higher efficiency can be obtained after the modified coupler is completely constructed.

4.4 Measurement of Attenuation in the Waveguides

For evaluating attenuation in the waveguide, several different techniques have been utilized. Takada [22] and Griffel [20] have used an optical fiber probe, which was connected at one end to a photodetector. Scanning the other end along the waveguide streak, they were able to measure the attenuation of the light in the waveguide. However, because the fiber tip is required to be placed in close proximity of the streak with high precision, this method is not convenient.

Also, another prism can be employed as an output coupler. By changing the distance between the input and the output prisms and measuring the output optical power, one can calculate attenuation in the waveguide. However, the accuracy of this technique greatly depends on the reproducibility of the output coupling efficiency, which is still a major drawback of the mechanical clamping system.

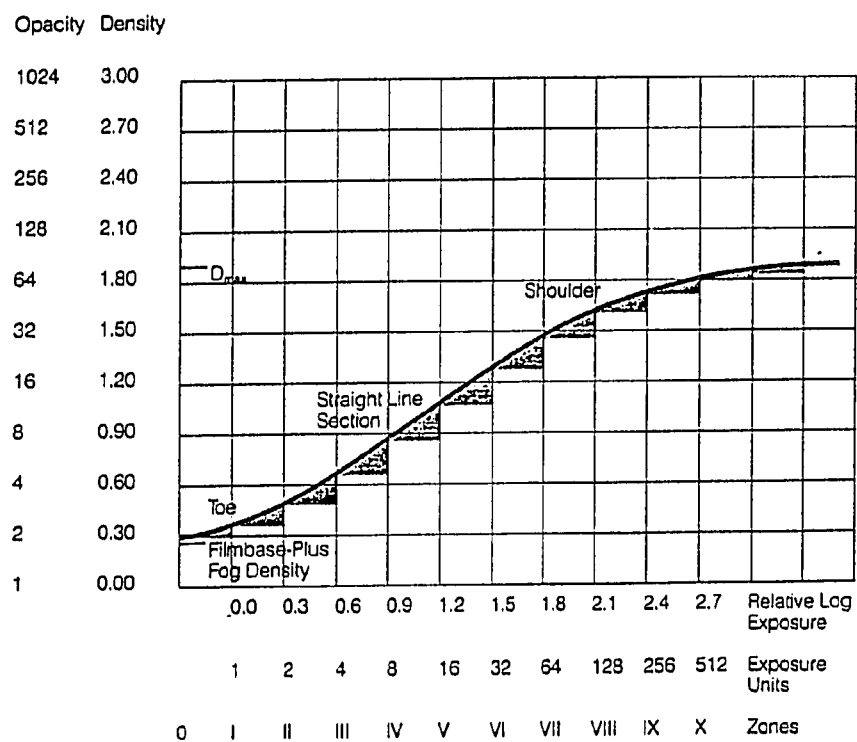


Figure 4.14 Characterization curve of the film sensitivity.

In our studies, a photographic method was used to record the surface scattered light intensity of the waveguiding streak [58]. Assuming the waveguide is homogeneous and the defects are uniformly distributed within and at the boundary of the waveguide, this technique is considered to be suitable for measuring the propagation attenuation without disturbing the testing setup. In order to obtain a wider field of view, only the input prism was used while the photographs were taken. The waveguiding streak was photographed for a number of different exposures. Referring to the characteristic curve of the film sensitivity, as shown in Figure 4.14, the linear region covers from Zone III to Zone VII [58]. Only the photographs taken within the linear region of the film sensitivity were used to calculate the propagation attenuation as well as the error. Projecting the photographs onto a screen, the relative intensities at various spots of the projected and magnified images were measured by a photometer with the sensor moving along the streak. The curves of relative intensity vs. waveguiding length are shown in Figures 4.15 through 4.18 and the regression lines computed by the least square method are also plotted in these figures. The zero on the horizontal axis coincides with the point in the waveguide adjacent to the input prism. The intensity of the point next to the prism is a little higher than that of the relative point on the regression line due to transmitted stray light from the prism and therefore data are not taken there. Data are not taken into account near the edge of the wafer since some reflection back from the edge might affect the measurement. However, these are minor factors since they are decaying as a function of $1/r$ and would not be linear in the logarithmic plots as shown in Figures 4.15 through 4.18. The attenuation was determined from the slope of the regression line. A picture of the waveguiding streak is shown in Figure 4.19. The picture was taken while the TM_2 mode was guided in the $LiNbO_3$ thin film with a thickness of $0.631\ \mu m$. The rutile prism is located at the left-hand side of the picture and covered by a piece of black paper for blocking off the stray light that may be unexpectedly captured by the camera.

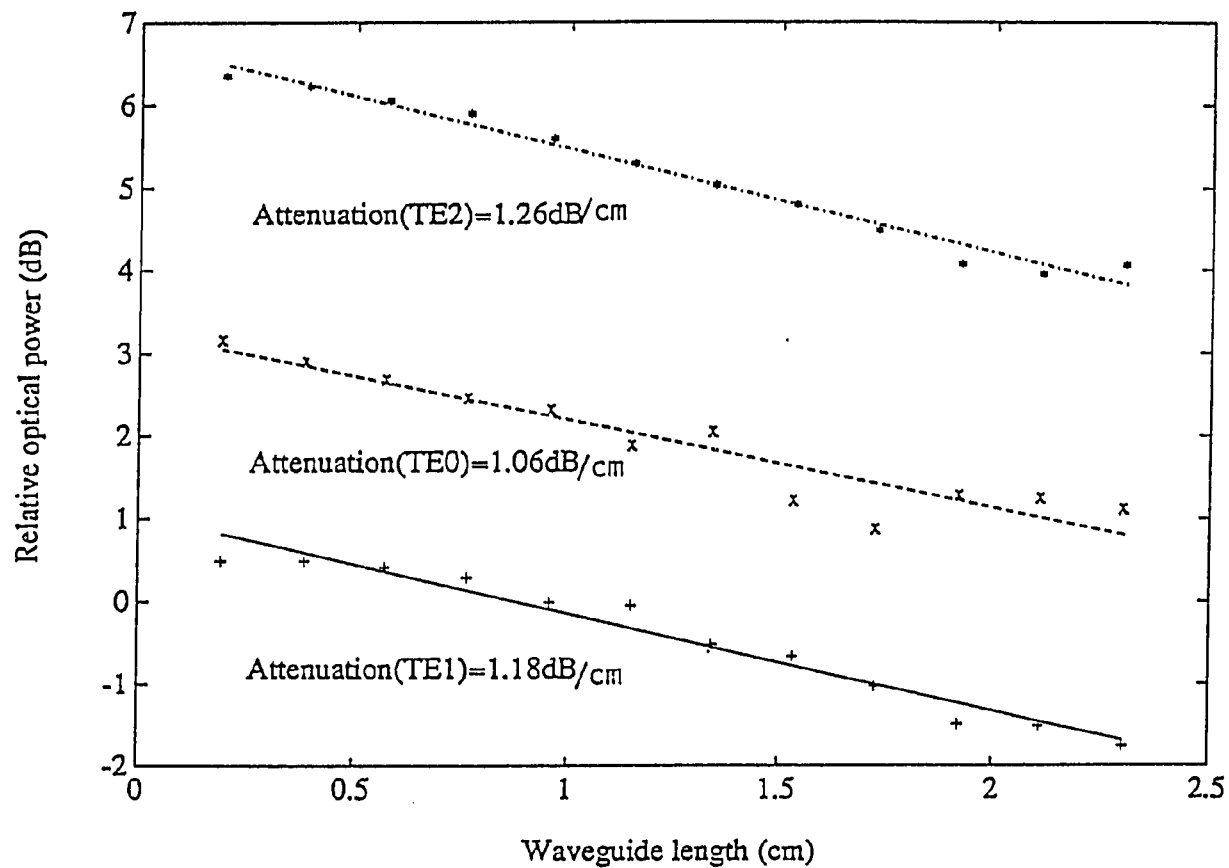


Figure 4.15 Surface-scattered light intensity of the TE modes of a LiNbO₃ waveguide on (001) sapphire measured by the photographic method as a function of distance along the waveguiding streak.

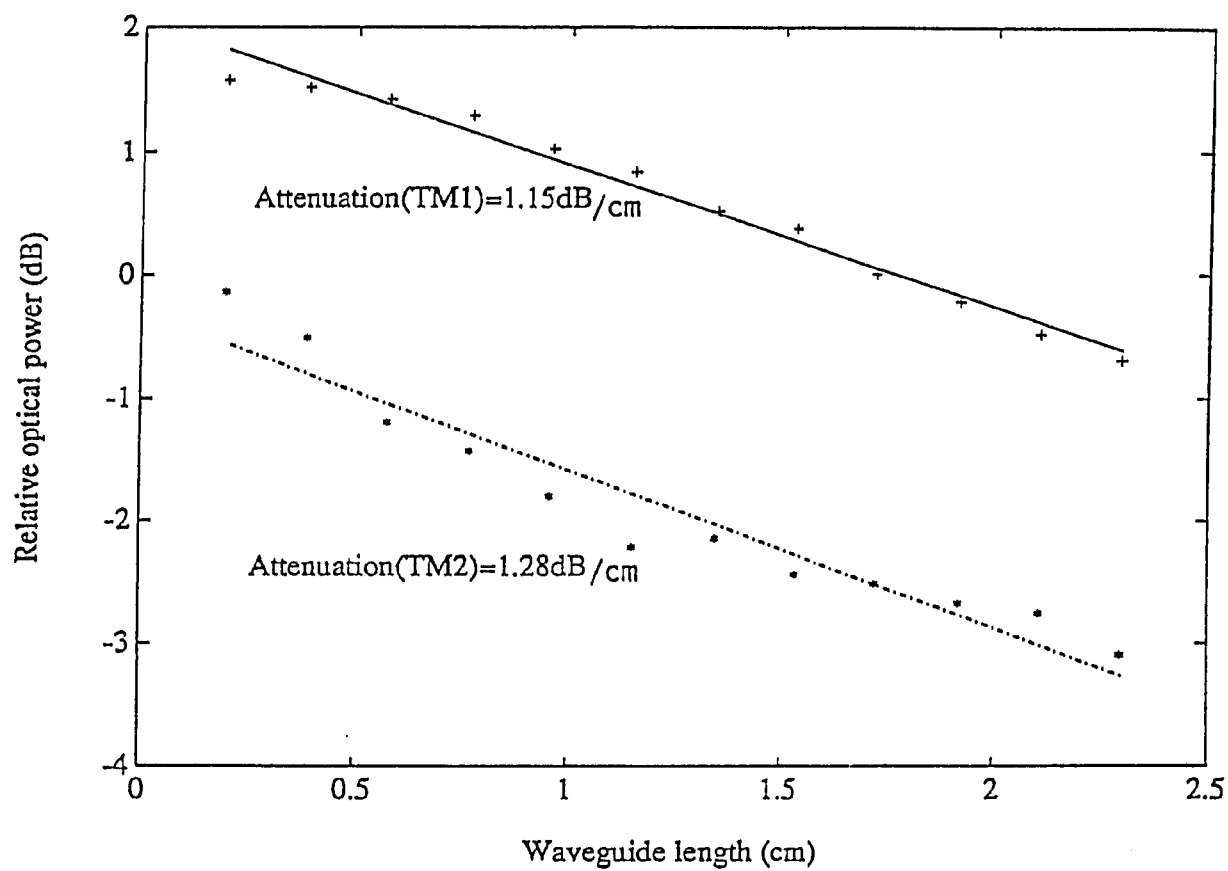


Figure 4.16 Surface-scattered light intensity of the TM modes of a LiNbO_3 waveguide on (001) sapphire measured by the photographic method as a function of distance along the waveguiding streak.

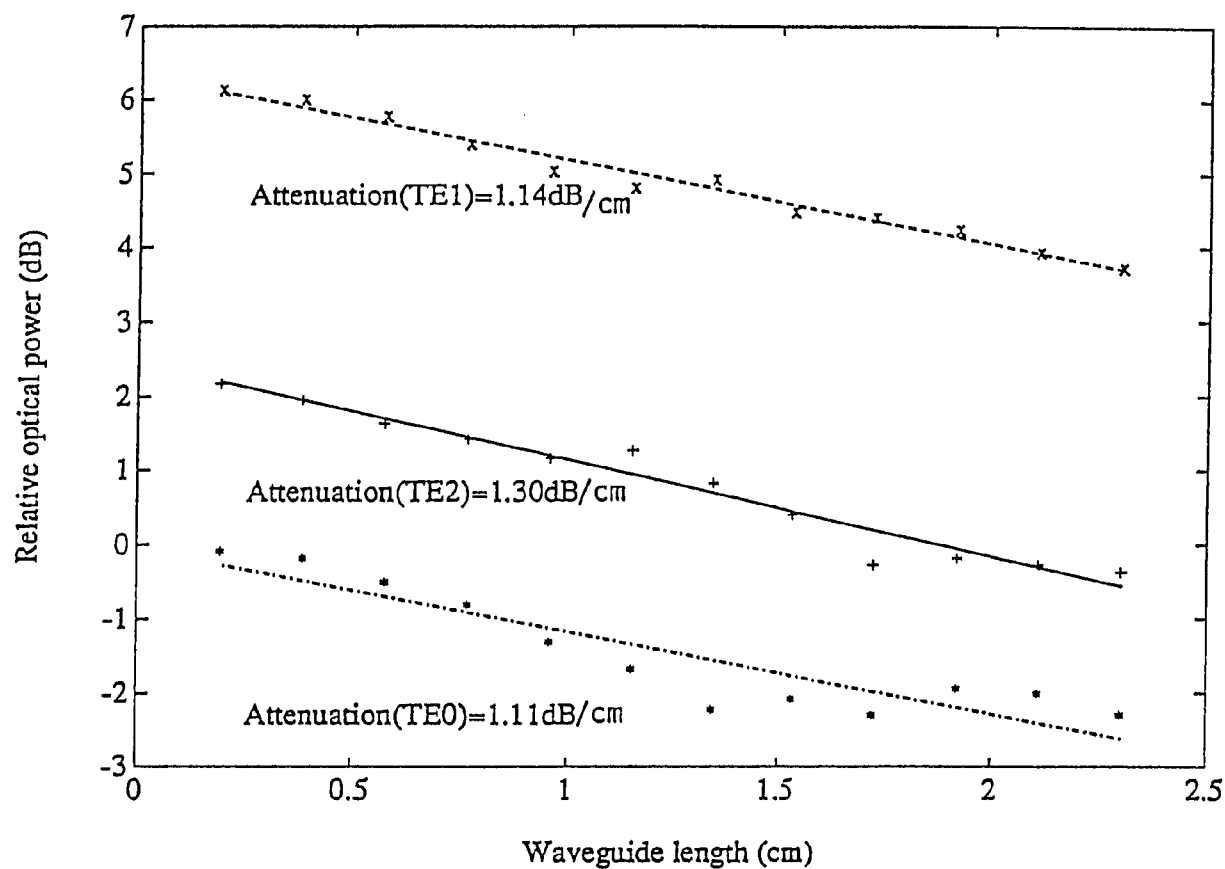


Figure 4.17 Surface-scattered light intensity of the TE modes of a LiNbO₃ waveguide on (110) sapphire measured by the photographic method as a function of distance along the waveguiding streak.

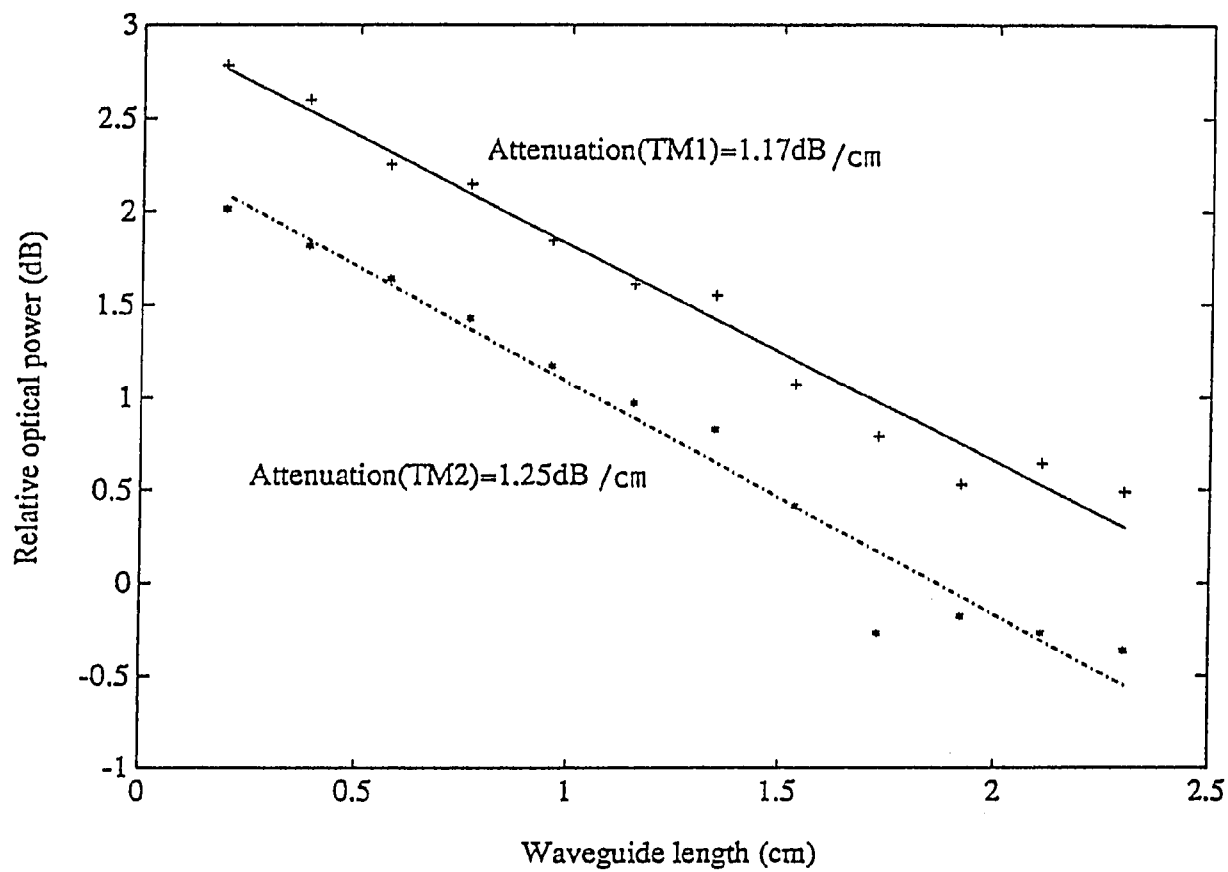


Figure 4.18 Surface-scattered light intensity of the TM modes of a LiNbO₃ waveguide on (110) sapphire measured by the photographic method as a function of distance along the waveguiding streak.

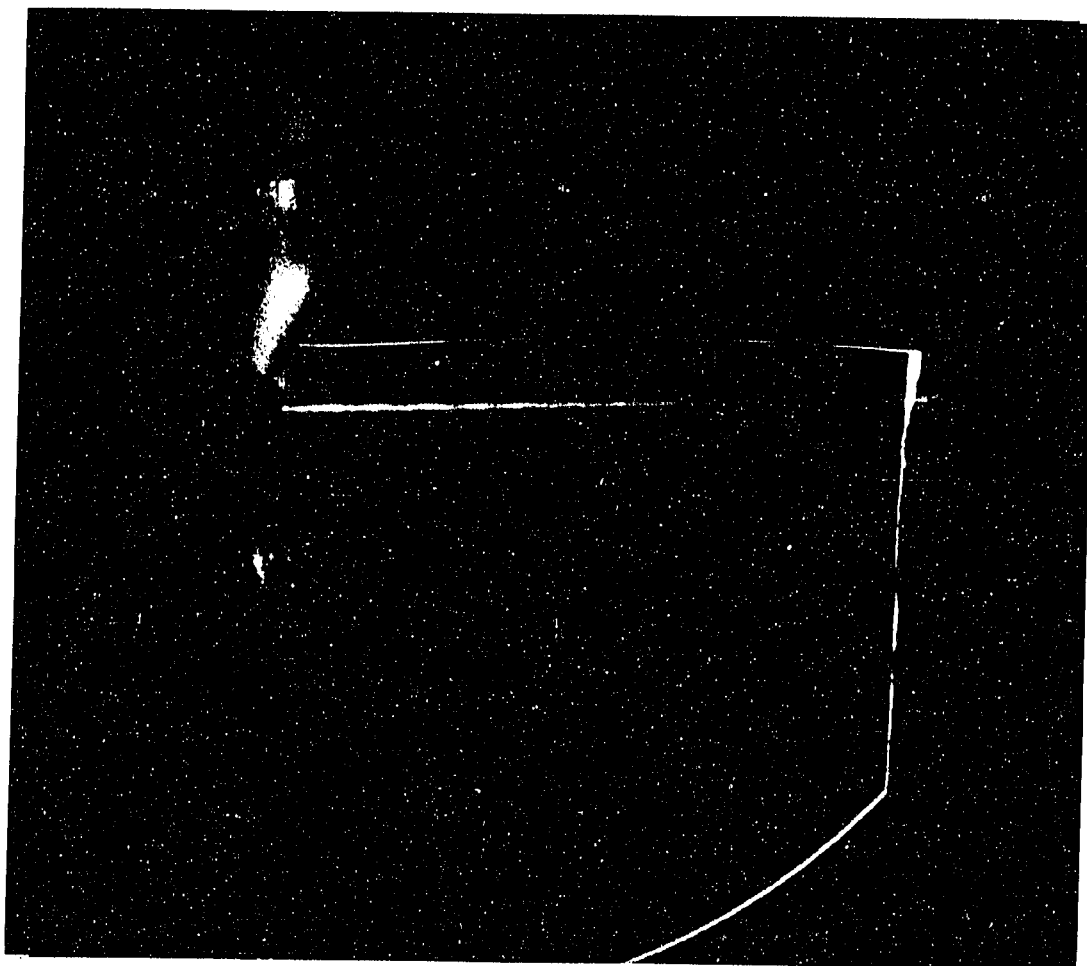


Figure 4.19 A 6328 \AA TM_2 mode was guided in the LiNbO_3 thin film. The rutile prism was clamped near the left edge of the waveguide. The guided streak was excited by the prism coupler and propagating from the left end to the right end of the waveguide.

Research group	Takada	Okada	Hewig
Year	1974	1976	1981
LiNbO ₃ target	disk	powder	powder
Substrate	sapphire	LiTaO ₃	glass
RF power	50 W	60 W	90-400 W
Target-substrate separation	4.0 cm	3.5 cm	
Gas pressure	20 mTorr	10 mTorr	20 mTorr
Substrate temperature	500°C	430°C	550°C
Deposition rate	250 Å/hr	500 Å/hr	1080-7200 Å/hr
Attenuation	9 dB/cm	8 dB/cm	3 dB/cm
Research group	Griffel	Griffel	Rice Univ.
Year	1985	1989	1990
LiNbO ₃ target	powder	powder	powder
Substrate	glass	glass	sapphire
RF power	150-700W		150W
Target-substrate separation			6 cm
Gas pressure	5 mTorr	10 mTorr	6 mTorr
Substrate temperature			580 C
Deposition rate			240 Å/hr
Attenuation	3-6 dB/cm	< 2 dB/cm	1.2 dB/cm

Table 4.6 Comparison of the attenuations measured by five research groups using different parameters in rf sputtering.

The attenuation in the rf-sputtered film was found to be in the range of 1.2 ± 0.1 dB/cm, which is very small compared to 9 dB/cm obtained by S. Takada [23], 8 dB/cm by A. Okada et al. [24], and 3 dB/cm by G.H. Hewig et al. [22]. These researchers used a similar sputtering technique to the one used here, while some of the parameters were different. Table 4.6 lists the different parameters used by these groups. The low rf power and the large target-substrate separation greatly lower the deposition rate, which produced a more uniform film with higher crystallinity. Since the attenuation is primarily caused by the scattering at the surface of the waveguide and at grain boundaries, crystalline quality is very important to effectively lower the attenuation of the film. Annealing techniques have been used by the previous research groups [21-24] because these processes can remove some of the defects in the films.

It is noticed that the waveguide tends to be more lossy for the higher order modes. This can be explained by the ray-optic picture in which the light ray bounces back and forth from the boundaries more frequently in the higher order modes than in the lower order ones, so that the light propagating in the higher order mode has more chance to be absorbed by the defects in the waveguide as well as to be scattered by the the boundary surfaces. Moreover, from the field theory, the optical energy density is distributed more in the core region of the waveguide for the lower order modes than for the higher order ones. In other words, the optical field of the lower order modes has weaker interaction with the waveguide boundary. Therefore, the propagation loss due to surface scattering is reduced and the light wave is better confined in the waveguide for the lower order modes.

Although the attenuation of 1.2 dB/cm obtained in this work is the lowest value reported for the sputtered thin film waveguides, it is still not as low as that of the waveguides made by thermal diffusion techniques [13,59]. In general, a value of 0.01 dB/cm can be achieved using the thermal diffusion method. To lower the attenuation of the films fabricated by rf sputtering, one must improve the optical uniformity of the film and its surface as well as reduce absorption in the film. Annealing, mechanochem-

ical polishing, and ion-beam etching are promising techniques for further reducing the attenuation.

The waveguide losses listed in Table 4.6 are all much smaller than the value of 40 dB/cm reported by B.J.Curtis and H.R.Brunner [59], who used chemical vapour deposition method (CVD) to grow the lithium niobate thin films. Other fabrication methods involving MBE (molecular beam epitaxy) and EGM (epitaxial growth by melting) have been tried to make low loss LiNbO_3 thin film optical waveguides. However, only 15.7 ± 0.8 dB/cm was obtained by using MBE [61], and no attenuation was reported for EGM [62]. Obviously, sputtering is a better method than these for growing low-loss thin film optical waveguides.

Chapter 5

Conclusions

5.1 Prism Coupler

To examine the optical properties of the as-sputtered LiNbO_3 thin film waveguides, beam coupling into the film is necessary. If the coupling efficiency is not of major interest, the single-prism coupler as shown in Figure 3.9 is the simplest and least damaging way of measuring the refractive index and the effective thickness of the waveguide in comparison to the other configurations shown in Figure 3.4 through 3.11. A coupling efficiency of about 20 % was the maximum value obtained for this geometry. However, for evaluating the attenuation of the light in the waveguide, a higher coupling efficiency is required such that the waveguiding streak is detectable by a camera. Techniques for increasing the net coupling efficiency involve simulating the optimum gap profile or making the coupling zone close to the vertical edge (the 90° angle) of the prism to minimize the out-coupling which occurs next to the in-coupling position. However, the second method has some problems, as described in the following, which may or may not be solved:

1. The irreproducibility due to the dust particles of random distribution and size. This problem can be corrected by inserting a spacer which not only eliminates the problem caused by the random particles, but also increases the coupling efficiency.
2. The impairment of the waveguide due to the sharp edge of the prism directly pressed on the waveguide with a large pressure. The problem may be removed by the same technique described above.

3. The damage of the vertical edge of the prism makes the prism unusable. Since this damage is unrepairable, this is considered to be the major disadvantage of this configuration.

To avoid the damage problem, the configuration of the single-prism coupler was modified into a new geometry, as shown in Figure 3.11, which keeps the 90° angle away from the waveguide and utilizes the optimum gap profile to produce a higher coupling efficiency. With this configuration, most of the disadvantages of the single- and two-prism coupler may be greatly eliminated. The accuracy and precision of the refractive index measurements made via the prism coupler are within ± 0.002 , which is much better than that of other conventional methods.

Another advanced technique for measuring the refractive index and the thickness of a thin film is ellipsometry. However, preknowledge of the range of the thickness is required due to the periodicity of the tabulated data. Also, the effects of the optical activity and birefringence of the films as well as those of the substrate are unknown, so that it is not simple to measure these optical parameters of a birefringent waveguide by ellipsometry.

5.2 Crystallinity of the Sputtered Films

XRD has been used to examine the crystallinity of the sputtered lithium niobate films on various oriented sapphire substrates. XRD scans have been demonstrated in Figures 4.1 through 4.4. For the (001) sample, (006) and (00 12) lithium niobate peaks show that the *c* axis of the film is normal to the surface. For the (110) sample, (110) and (220) lithium niobate peaks show that the *c* axis of the film is in the plane of the surface. Distortion of the lithium niobate unit cells was observed for the (001) sample due to the large lattice mismatch. The XRD studies assure that the sputtered lithium niobate films are highly oriented polycrystalline.

5.3 Refractive Index and Thickness

A He-Ne laser beam was successfully fed, by the prism coupler, into the LiNbO_3 waveguides sputtered on sapphire substrates with various orientations and the curves of reflected intensity vs. incidence angle were plotted to determine the mode angles. Corrections have been made to recover the mode angles from their shifted positions due to the tilting of the curves. The refractive indices and the thicknesses were then calculated by making use of the corrected mode angles. The refractive indices and thicknesses of the films measured in these studies are tabulated in Table 4.3. The systematic errors were also calculated to be $\pm 0.001 \mu\text{m}$ and ± 0.002 for thickness and refractive index, respectively.

The effective thicknesses were then used to calculate the deposition rate which was determined to be about 240 \AA/hr . Such a low deposition rate was due to the low rf power (150W) and the large separation (6 cm) between the target and the substrate. Certainly, the dependence of the deposition rate vs. rf power or separation, depends on the individual sputtering system used. Since the thickness is a function of sputtering time, some passive devices can be made by controlling the sputtering time. For instance, thin film lens can be fabricated by making use of a mask equipped by a stepper motor and then creating a gradual film thickness change.

Since the sputtered films exhibit birefringence, they are determined to be highly oriented polycrystalline, which is consistent with the XRD data. However, the fully understanding to the relationship between the refractive index of TE or TM wave and that of ordinary or extraordinary ray requires knowledge of the angle between the orientation of the c axis of the film and the propagation direction and the polarization of the guided light [63]. Therefore, only the index of TE and TM modes propagating in the (001) sample can now be exactly related to the indices of ordinary and extraordinary rays, respectively. According to Table 4.4, $n_o = n_{TE} = 2.322$ and $n_e = n_{TM} = 2.263$ at $\lambda = 6328 \mu\text{m}$. These values are very close to but slightly higher

than the bulk values. They are also close to the values measured by Takada ($n_o = 2.32 \pm 0.02$ and $n_e = 2.18 \pm 0.04$) and Okada ($n_o = 2.318$).

5.4 Attenuation

The attenuation of the light in the LiNbO_3 thin films was evaluated by the photographic method. It is noticed that the higher order modes have a higher value of attenuation because the scattering occurs more frequently at the interfaces for the higher order modes and the absorption in the waveguide is increased for a longer optical path. The comparison of the attenuation constants obtained by several research groups are shown in Table 4.5. The attenuation for different modes in the waveguide was estimated to be 1.2 dB/cm, which is smaller than the previously published values. The low deposition rate in our case is a major factor for effectively reducing the defects in the films, thereby reducing absorption of optical energy in the waveguide and producing an optically smooth surface and thus reducing the scattering at the surface of the waveguide.

Although the attenuation reported in this thesis is the lowest value reported for the sputtered lithium niobate films, it is still not comparable to the value of 0.5 dB/cm which can be easily obtained for a Ti-diffused waveguide [13,60]. The greatest advantage of the thermal diffusion method is its making use of the well-polished bulk material surface to be the surface of the waveguide and the uniformity of the diffusion layer such that there is no lattice constant mismatch at the guide-substrate interface. Therefore, the attenuation caused by scattering at the boundary of the waveguide is greatly reduced. However, the requirement of using bulk material also places some limitations on the applications of the diffused waveguides. For instance, the diffused waveguides can not make use of special properties of other optical materials by simply putting them together as in multi-layer structures.

For minimizing the attenuation in the sputtered thin film waveguides, the substrates can be mechanochemically polished and the sputtered films can be ion-beam

etched to yield a better surface uniformity. Also, annealing treatments can be applied to remove the crystalline defects so as to reduce the absorption in the waveguide and the scattering at the boundary.

The low attenuation obtained in this research assures that the growth of the thin films by rf sputtering method is a promising technique for making low loss optical waveguides. Moreover, the usefulness of OICs (Optical Integrated Circuits) is not derived from signal processing using optically energetic pulses, but comes instead from utilizing the wave characteristics of optical signals. Therefore, the requirement of low attenuation for optical waveguiding is very important for building OICs. With the low-loss lithium niobate waveguides reported here, a great number of devices such as power dividers, directional couplers, phase modulators, TIR switches, mode converters, frequency doublers, etc., is made possible. Moreover, because of the extremely large electro-optic coefficient of lithium niobate and single-mode waveguide structure, gaps in controlling electrodes can be reduced, which makes lower voltage operation and more compact devices possible.

5.5 Future Research

5.5.1 Optical properties and fabrication techniques

This work has shown that high optical quality LiNbO_3 thin film waveguides can be grown on crystalline sapphire by rf sputtering. Since propagation attenuation must be kept to a minimum in waveguides, a continuing effort has to be made to reduce optical losses in lithium niobate films for OIC applications. An understanding of the relationship between the controllable sputtering parameters and optical losses must be fully quantified. Other important properties of lithium niobate films, such as electro-optic and acousto-optic coefficients, need to be fully investigated in order to develop new devices. Furthermore, the techniques for fabricating channel waveguides

must be explored before building devices. The results of this research will then be applied to building actual optical processing devices.

5.5.2 Devices

Optical power density is extremely large in waveguides compared with that of optical beams in free space. Optical nonlinear effects, therefore, can be utilized for device-making. For example, using second harmonic generation, a frequency doubler can be built as shown by Hewig [21]. Utilization of higher order multiphoton effects such as optical mixing and parametric amplification can be studied in these waveguide structures. Making use of electro-optic or acousto-optic effect, an optical modulator or switch can also be constructed. Because of the capability of concentrating both the optical wave and the modulating field in a very small region, waveguide modulators and switches are much more efficient than their bulk counterparts.

5.5.3 Combination of Optical IC and Semiconductor IC

X-ray diffraction has shown that highly oriented polycrystalline LiNbO_3 can be grown on silicon if the silicon substrate has the (111) orientation. Because the refractive index of silicon is greater than that of lithium niobate and silicon is a semiconductor, it is required to grow a silicon dioxide buffer layer between the lithium niobate thin film and the silicon substrate. Of particular significance, this is the first effort to combine the optical processing capability of lithium niobate with the electronic processing capability of silicon. Further efforts will be made to extend the capability of growing thin film crystalline LiNbO_3 on other structures and materials to utilize its optical, dielectric, and acoustic properties.

Bibliography

- [1] N. S. Kapany and J. J. Burke, Optical Waveguides, New York: Academic Press, (1972).
- [2] M. K. Barnoski, Introduction to Integrated Optics, New York: Plenum Press, (1974).
- [3] D. Marcuse, Theory of Dielectric Optical Waveguides, New York: Academic Press, (1974).
- [4] Z. Knittl, Optics of Thin Films, London: John Wiley & Sons, (1976).
- [5] P. K. Tien, "Integrated Optics and New Wave Phenomena in Optical Waveguides," Review of Modern Physics, (1977).
- [6] T. Tamir, Integrated Optics, 2nd edition, Topics Appl. Phys., vol.7, Berlin: Springer-Verlag, (1979).
- [7] G. H. Owyang, Foundations of Optical Waveguides, New York: Elsevier, (1981).
- [8] M. J. Adams, An Introduction to Optical Waveguides, New York: John Wiley & sons, (1981).
- [9] S. Martellucci and A. N. Chester, Integrated Optics: Physics and Applications, New York: Plenum Press, (1981).
- [10] A. Yariv and P. Yeh, Optical Waves in Crystals, New York: John Wiley & Sons, (1984).

- [11] H. A. Haus, Waves and Fields in Optoelectronics, New Jersey: Prentice-Hall, (1984).
- [12] D. L. Lee, Electromagnetic Principles of Integrated Optics, New York: John Wiley & Sons, (1986).
- [13] T. Tamir, Guided-Wave Optoelectronics, Berlin: Springer-Verlag, (1988).
- [14] J. C. Burfoot, Ferroelectrics: An Introduction to the Physical Principles, London: D. Van Nostrand, (1967).
- [15] M. E. Lines and A. M. Glass, Principles and Applications of Ferroelectrics and Related Materials, Oxford University Press, (1977).
- [16] J. L. Vossen and W. Kern, Thin Film Processes, New York: Academic Press, (1978).
- [17] R. S. Weis and T. K. Gaylord, "Lithium Niobate: Summary of Physical Properties and Crystal Structure," Appl. Phys. A37, pp. 191-203, (1985).
- [18] T. Cholapranee, T. A. Rabson, and L. Fabiny, "Properties of Lithium Niobate Thin Polycrystalline Films Deposited on Silicon Substrates," Proceedings of Sixth IEEE International Symposium on Applications of Ferroelectrics (ISAF '86), Bethlehem, PA, pp. 585-588, (1986).
- [19] D. Bondurant and F. Gnadinger, "Ferroelectric for Nonvolatile RAMs," IEEE Spectrum, pp. 30-33, July, (1989).
- [20] L. H. Parker and A. F. Tasch, "Ferroelectric Materials for 64 M6 and 256 M6 DRAMs," IEEE Circuits and Devices Magazine, pp. 17-26, January, (1990).
- [21] G. Griffel, S. Ruschin, and N. Croitoru, "Linear Electro-Optic Effect in Sputtered Polycrystalline LiNbO₃ Films," Appl. Phys. Lett., vol. 54, no. 15, pp. 1385-1397, (1989).

- [22] G. H. Hewig and K. Jain, "Frequency Doubling in a LiNbO_3 Thin Film Deposited on Sapphire," J. Appl. Phys., vol. 54, no. 1, pp. 57-61, (1983).
- [23] S. Takada, M. Ohnishi, H. Hayakawa, and N. Mikoahiba, "Optical Wave-guides of Single-crystal LiNbO_3 Film Deposited by Rf Sputtering," Applied Optics, vol. 24, pp. 490-492, (1974).
- [24] A. Okada, "Optical Waveguiding Properties of Sputtered LiNbO_3 Single Crystal Thin Films on LiTaO_3 Substrates," Ferroelectrics, vol. 14, pp. 739-742, (1976).
- [25] S. M. SZE, VLSI technology, 2nd edition, New York: McGraw-Hill, (1988).
- [26] P. K. Tien, R. Ulrich, and R. J. Martin, "Modes of Propagating Light Waves in Thin Deposited Semiconductor Film," Applied Physics Letters, vol. 14, pp. 291-294, (1969).
- [27] J. H. Harris, R. Shubert, and J. N. Polky, "Beam Coupling to Films," J. Opt. Soc. Am., vol. 60, pp. 1007-1016, (1970).
- [28] A. Nussbaum and R. A. Phillips, Contemporary Optics for Scientists and Engineers, New Jersey: Prentice-Hall, pp. 349, (1976).
- [29] J. E. Goell and R. D. Standley, "Integrated Optical Circuits," Proceedings of the IEEE, vol. 58, pp. 1504-1512, (1970).
- [30] P. K. Tien and R. Ulrich, "Theory of Prism-Film Coupler and Thin-Film Light Guides," J. Opt. Soc. Am. vol. 60, pp. 1325-1337, (1970).
- [31] R. Ulrich, "Theory of the Prism-Film Coupler by Plane-Wave Analysis," J. Opt. Soc. Am., vol. 60, pp. 1337-1350, (1970).
- [32] R. Ulrich, "Optimum Excitation of Optical Surface Waves," J. Opt. Soc. Am., vol. 61, pp. 1467-1477, (1971).

- [33] P. K. Tien, "Light Wave in Thin Films and Integrated Optics," *Appl. Opt.*, vol. 10, pp. 2395-2413, (1971).
- [34] P. K. Tien, G. Smolinsky, and R. J. Martin, "Thin Organosilicon Films for Integrated Optics," *Appl. Opt.*, vol. 11, pp. 637-642, (1972).
- [35] H. P. Weber, F. A. Dunn, and W. N. Leibolt, "Loss Measurements in Thin-Film Optical Waveguides," *Appl. Opt.*, vol. 12, pp. 755-757, (1973).
- [36] R. J. Bell, B. Fischer, and I. L. Tyler, "Coupling to Surface Waves with Prisms via Attenuated Total Reflection," *Appl. Opt.*, vol. 12, pp. 832-836, (1973).
- [37] R. Ulrich, "Frequency-Selective Beam Coupler for Integrated Optics," *Appl. Phys. Lett.*, vol. 24, pp. 21-24, (1974).
- [38] R. Ulrich and R. Torge, "Measurement of Thin Film Parameters with a Prism Coupler," *Appl. Opt.*, vol. 12, pp. 2901-2908, (1973).
- [39] R. Ulrich and D. Chen, "Offset Prism for Optical Waveguide Coupling," *Appl. Opt.*, vol. 13, pp. 1850-1852, (1974).
- [40] G. L. Tangonan, M. K. Barnoski, and A. Lee, "Tapered Gap Prism Couplers for High Index Materials," *Appl. Opt.*, vol. 16, pp. 1795-1796, (1977).
- [41] D. Sarid and D. Kermisch, "Prism-Waveguide Coupling Efficiency for Waveguides with an Arbitrary Refractive-Index Profile," *Appl. Phys. Lett.*, vol. 33, no. 7, pp. 619-620, (1978).
- [42] D. Sarid, P. J. Cressman, and R. L. Holman, "High-Efficiency Prism Coupler for Optical Waveguides," *Appl. Phys. Lett.*, vol. 33, no. 6, pp. 514-515, (1978).
- [43] D. Sarid, "High-Efficiency Input-Output Prism Waveguide Coupler : an Analysis," *Appl. Opt.*, vol. 18, pp. 2921-2926, (1979).

- [44] R. L. Holman and P. J. Cressman, "Practical Aspects of Efficient Tapered-Gap Prism Coupling to Diffused Lithium Niobate Optical Waveguides," *Ferroelectrics*, vol. 27, pp. 85-88, (1980).
- [45] Y. H. Won, P. C. Jaussaud, and G. H. Chartier, "Three-Prism Loss Measurements of Optical Waveguides," *Appl. Phys. Lett.*, vol. 37, no. 3, pp. 269-271, (1980).
- [46] Z. Yin and B. K. Garside, "Low-Loss GeO_2 Optical Waveguide Fabrication Using Low Deposition Rate Rf Sputtering," *Appl. Opt.*, vol. 21, no. 23, (1982).
- [47] S. Sriram, W. D. Partlow, and C. S. Liu, "Low-Loss Optical Waveguides Using Plasma-Deposited Silicon Nitride," *Appl. Opt.*, vol. 22, no. 23, pp. 3664-3665, (1983).
- [48] M. J. Li, M. P. De Micheli, D. B. Ostrowsky, and M. Papuchon, "High Index Low Loss LiNbO_3 Waveguides," *Opt. Comm.*, vol. 62, no. 1, pp. 17-20, (1987).
- [49] S. Morasca and C. De Bernardi, "High Accuracy Determination of Semiconductor Substrate and Waveguide Refractive Index by Prism Coupling," *SPIE*, vol. 993, *Integrated Optical Circuit Engineering VI*, pp. 164-166, (1988).
- [50] E. Pelletier, F. Flory, and Y. Hu, "Optical Characterization of Thin Films by Guided Waves," *Appl. Opt.*, vol. 28, no. 14, pp. 2918-2924, (1989).
- [51] L. V. Iogansen, "Theory of Resonant Electromagnetic Systems That Use Total Internal Reflection," *Soviet Physics-Technical Physics*, vol. 7, pp. 295-303, (1962).
- [52] L. V. Iogansen, "Theory of Resonant Electromagnetic Systems with Total Internal Reflection, II," *Soviet Physics-Technical Physics*, vol. 8, pp. 985-988, (1964).

- [53] L. V. Iogansen, "Theory of Resonant Electromagnetic Systems with Total Internal Reflection, III," *Soviet Physics-Technical Physics*, vol. 11, pp. 1529-1534, (1967).
- [54] J. E. Midwinter, "Theory of an Ultra-Broad-Band Optical Dielectric Waveguide Coupler System," *IEEE J. Quan. Elec.*, vol. QE-7, pp. 345-350, (1971).
- [55] H. Osterberg and W. L. Smith, "Transmission of Optical Energy Along Surfaces: Part I, Homogeneous Media," vol. 54, pp. 1073-1078, (1964).
- [56] H. Osterberg and W. L. Smith, "Transmission of Optical Energy Along Surfaces: Part II, Inhomogeneous Media," vol. 54, pp. 1078-1084, (1964).
- [57] D. P. Koistinen and R. E. Marburger, *Trans. ASM*, vol. 51, p. 537, (1959).
- [58] A. Adams, The Negative, Boston: Little, Brown and Company, (1981).
- [59] B. J. Curtis and H. R. Brunner, "The Growth of Thin Films of Lithium Niobate by Chemical Vapour Deposition," *Mat. Res. Bull.*, vol. 10, no. 6, Pergamon Press, pp. 515-520, (1975).
- [60] H. Nishihara, M. Haruna, and H. Suhara, Optical Integrated Circuits, New York: McGraw-Hill, (1989).
- [61] R. A. Betts and C. W. Pitt, "Growth of Thin-Film Lithium Niobate by Molecular Beam Epitaxy," *Elec. Lett.*, vol. 21, no. 21, pp. 960-962, (1985).
- [62] S. Miyazawa, "Growth of LiNbO_3 Single-Crystal Film for Optical Waveguides," *Appl. Phys. Lett.*, vol. 23, no. 4, pp. 198-200, (1973).
- [63] A. Knoesen, T. K. Gaylord, and M. G. Moharam, "Hybrid Modes in Uniaxial Planar Waveguides," *J. Lightwave Technology*, vol. 6, no. 6, pp. 1083-1104, (1988).

Appendix A

```

/*      This program calculates the refractive index and thickness of the      */
/* waveguide. At least two mode angles are required to run the program.      */
/* Standard deviation will be given if more than two data are entered into   */
/* the program.                                                                */

#include <math.h>          /*include math functions*/
#include <stdio.h>         /*include input/output functions*/
#define pi 3.141592654
#define lambda 0.0000006328
#define TEmode 0
#define TMmode 1
#define maxdeltanum 20

double alphapr,npr,ns,n0;
double thetfa[maxdeltanum],delta[maxdeltanum];
int    mode[maxdeltanum];
int    polarization;
int    deltanum;

enter_parameters()
{
    float temp;
    int    i;

    n0 = 1.000;
    printf("This program determines the Film Index nf and Thickness d\n");
    printf(" from the measured coupling angles for two or more modes.\n\n");
    printf("\n\nPolarization (TE=%d,TM=%d): ",TEmode,TMmode);
    scanf("%d",&polarization);
    printf("Number of measured coupling angles delta: ");
    scanf("%d",&deltanum);
    for (i=1;i<=deltanum;++i) {
        printf("mode number[%d]: ",i);
        scanf("%d",&(mode[i]));
        if (polarization == TEmode)
            printf("delta for TE%d [%d] (in degrees): ",mode[i],i);
        else
            printf("delta for TM%d [%d] (in degrees): ",mode[i],i);
        scanf("%f",&temp);
        delta[i] = temp*pi/180.0;
    }
    if (polarization == TEmode) {
        printf("Prism angle (in degrees): ");
        scanf("%f",&temp);
        alphapr = pi/180.0*temp;
        printf("Prism refractive index (usu. 2.8659): ");
        scanf("%f",&temp);
        npr = temp;
    }
    else {
        polarization = TMmode;
        printf("Prism angle (in degrees): ");
        scanf("%f",&temp);
        alphapr = pi/180.0*temp;
        printf("Prism refractive index (usu. 2.5839): ");
        scanf("%f",&temp);
        npr = temp;
    }
    printf("Substrate index (Sapphire = 1.77, SiO2 = 1.46): ");
    scanf("%f",&temp);
    ns = temp;
    printf("\n");
}

/*This is the function we wish to find the root of */

```

```

double zTE(t,Nf1,Nf2,p1,p2)
double t;
double Nf1,Nf2;
int p1,p2;
{
    double zout;

    zout = (1.0/sqrt(t*t-Nf1*Nf1))*((double)p1*pi + atan2(sqrt(Nf1*Nf1-1.0),sqrt(t*t-Nf1*Nf1)
        - (1.0/sqrt(t*t-Nf2*Nf2))*((double)p2*pi + atan2(sqrt(Nf2*Nf2-1.0),sqrt(t*t-Nf2*Nf2)
    return(zout);
}

```

```

double zTM(t,Nf1,Nf2,p1,p2)
double t;
double Nf1,Nf2;
int p1,p2;
{
    double zout;

    zout = (1.0/sqrt(t*t-Nf1*Nf1))*((double)p1*pi + atan2(t*t*sqrt(Nf1*Nf1-1.0),sqrt(t*t-Nf1
        - (1.0/sqrt(t*t-Nf2*Nf2))*((double)p2*pi + atan2(t*t*sqrt(Nf2*Nf2-1.0),sqrt(t*t-Nf2
    return(zout);
}

```

/*This is the main routine*/

```

main()
{
    double nf[maxdeltanum],d[maxdeltanum];
    double nfaverage,daverage;
    double nfstd,dstd;
    int i;

    enter_parameters();

    nfaverage = 0.0;
    daverage = 0.0;
    nfstd = 0.0;
    dstd = 0.0;
    for (i=1;i<=deltanum-1;++i) {
        iterate(delta[i],delta[i+1],mode[i],mode[i+1],&(nf[i]),&(d[i]));
        d[i] *= 1000000.0;
        nfaverage += nf[i];
        daverage += d[i];
        nfstd += nf[i]*nf[i];
        dstd += d[i]*d[i];
    }
    nfaverage = nfaverage/((double)(deltanum-1));
    daverage = daverage/((double)(deltanum-1));
    nfstd = nfstd/((double)(deltanum-1)) - nfaverage*nfaverage;
    dstd = dstd/((double)(deltanum-1)) - daverage*daverage;
    printf("nf = %f with standard deviation = %f\n",nfaverage,nfstd);
    printf("d = %f microns with standard deviation = %f\n",daverage,dstd);
}

```

```

iterate(delta1,delta2,p1,p2,nf,d)
double delta1,delta2;
int p1,p2;
double *nf,*d;
{
    double Nf1,Nf2;
    double t1,t2,z1,z2,t,tnew,znew;

```

```

Nf1 = npr*sin(asin((1.0/npr)*cos(pi/2.0 - delta1)) + alphapr);
Nf2 = npr*sin(asin((1.0/npr)*cos(pi/2.0 - delta2)) + alphapr);

if (Nf1 > Nf2)
    t1 = Nf1 + 0.00000001;
else
    t1 = Nf2 + 0.00000001;
t2 = 20.0;

if (polarization == TEmode) {
    z1 = zTE(t1,Nf1,Nf2,p1,p2);
    z2 = zTE(t2,Nf1,Nf2,p1,p2);
}
if (polarization == TMmode) {
    z1 = zTM(t1,Nf1,Nf2,p1,p2);
    z2 = zTM(t2,Nf1,Nf2,p1,p2);
}
while (z1*z1 > 0.000000001) { /*continue searching for root until*/
    /* tolerance is reached*/
    tnew = 0.5*(t1+t2); /*use midpoint of interval as next guess*/
    if (polarization == TEmode)
        znew = zTE(tnew,Nf1,Nf2,p1,p2);
    else
        znew = zTM(tnew,Nf1,Nf2,p1,p2);
    if (znew*z1 > 0.0) { /*choose interval which the root lies in*/
        /* and form new interval*/
        z1 = znew;
        t1 = tnew;
    }
    else {
        z2 = znew;
        t2 = tnew;
    }
}
/* printf("z = %f, t = %f\n",z1,t1); */ /*output results: z = value of function at*/
/* t = approximate location of the root*/

*nf = tnew;
if (polarization == TEmode) {
    *d = (lambda/(2.0*pi*sqrt(tnew*tnew-Nf1*Nf1)))*(p1*pi + atan2(sqrt(Nf1*Nf1-1.0),sqrt(
}
else {
    *d = (lambda/(2.0*pi*sqrt(tnew*tnew-Nf1*Nf1)))*(p1*pi + atan2(tnew*tnew*sqrt(Nf1*Nf1-
}
}

```

Appendix B

```

/*      This is the program for predicting the mode angles.  Estimated */
/* index of refraction and thickness are required for the calculation. */

#include <math.h>          /*include math functions*/
#include <stdio.h>         /*include input/output functions*/
#define pi 3.141592654
#define lambda 0.0000006328
#define TEmode 0
#define TMmode 1

double d,nfTE,nfTM,alphaPr,nprTE,nprTM,ns,n0;
int polarization;

enter_parameters()
{
    float temp;

    n0 = 1.000;
    printf("\n\nPolarization (TE=%d,TM=%d): ",TEmode,TMmode);
    scanf("%d",&polarization);
    if (polarization == TEmode) {
        printf("Film thickness (in microns): ");
        scanf("%f",&temp);
        d = 0.000001*temp;
        printf("Film refractive index (usu. 2.2 to 2.3263): ");
        scanf("%f",&temp);
        nfTE = temp;
        printf("Prism angle (in degrees): ");
        scanf("%f",&temp);
        alphaPr = pi/180.0*temp;
        printf("Prism refractive index (usu. 2.8659): ");
        scanf("%f",&temp);
        nprTE = temp;
    }
    else {
        polarization = TMmode;
        printf("Film thickness (in microns): ");
        scanf("%f",&temp);
        d = 0.000001*temp;
        printf("Film refractive index (usu. 2.2826): ");
        scanf("%f",&temp);
        nfTM = temp;
        printf("Prism angle (in degrees): ");
        scanf("%f",&temp);
        alphaPr = pi/180.0*temp;
        printf("Prism refractive index (usu. 2.5839): ");
        scanf("%f",&temp);
        nprTM = temp;
    }
    printf("Substrate index (Sapphire = 1.77, SiO2 = 1.46): ");
    scanf("%f",&temp);
    ns = temp;
    printf("\n");
}

/*This is the function we wish to find the root of */
double zTE(t,mode)
double t;
int mode;
{
    double zout;

    zout = 2.0*(double)mode*pi - 2.0*pi*nfTE/lambda*2.0*d*cos(t)
        + 2.0*atan2(sqrt(nfTE*nfTE*sin(t)*sin(t) - n0*n0),(nfTE*cos(t)))

```

```

        + 2.0*atan2(sqrt(nfTE*nfTE*sin(t)*sin(t) - ns*ns), (nfTE*cos(t)));
    return(zout);
}

double zTM(t,mode)
double t;
int mode;
{
    double zout;

    zout = 2.0*(double)mode*pi - 2.0*pi*nfTM/lambda*2.0*d*cos(t)
        + 2.0*atan2(nfTM*sqrt(nfTM*nfTM*sin(t)*sin(t) - n0*n0),cos(t))
        + 2.0*atan2(nfTM*sqrt(nfTM*nfTM*sin(t)*sin(t) - ns*ns),ns*ns*cos(t));
    return(zout);
}

/*This is the main routine*/
main()
{
    int mode;
    int valid;
    double deltaTE;
    double deltaTM;
    double deltacriticalTE;
    double deltacriticalTM;

    enter_parameters();

    if (polarization == TEmode) {
        for (mode=0,valid=1;valid;++mode) {
            iterate(mode,&deltaTE,&valid);
            if (valid)
                printf("TE%d = %f\n",mode,deltaTE*180.0/pi);
        }
    }
    else {
        for (mode=0,valid=1;valid;++mode) {
            iterate(mode,&deltaTM,&valid);
            if (valid)
                printf("TM%d = %f\n",mode,deltaTM*180.0/pi);
        }
    }
}

iterate(mode,delta,valid)
int mode;
double *delta;
int *valid;
{
    double t1,t2,z1,z2,t,tnew,znew;

    /*printf("Bisection Method\n");*/
    /*printf("enter tmin:\n");*/
    /*scanf("%f",&t);*/
    if (polarization == TEmode)
        t1 = asin(ns/nfTE) + 0.0001;
    else
        t1 = asin(ns/nfTM) + 0.0001;
    /*printf("enter tmax:\n");*/
    /*scanf("%f",&t);*/
    t2 = pi/2.0 - 0.0001;
    /*lower bound where root can be found*/
    /*upper bound where root can be found*/
}

```

```

if (polarization == TEmode) {
    z1 = zTE(t1,mode);
    z2 = zTE(t2,mode);
}
/*evaluate function at left bound*/
/* and at right bound*/
if (polarization == TMmode) {
    z1 = zTM(t1,mode);
    z2 = zTM(t2,mode);
}
if (z1*z2 >= 0.0)
    *valid = 0;
else {
    *valid = 1;
    while (z1*z1 > 0.000000001) {
        /*continue searching for root until*/
        /* tolerance is reached*/
        /* printf("%f %f %f %f\n",z1,z2,t1,t2); */
        tnew = 0.5*(t1+t2); /*use midpoint of interval as next guess*/
        if (polarization == TEmode)
            znew = zTE(tnew,mode);
        else
            znew = zTM(tnew,mode);
        if (znew*z1 > 0.0) {
            /*choose interval which the root lies in*/
            /* and form new interval*/
            z1 = znew;
            t1 = tnew;
        }
        else {
            z2 = znew;
            t2 = tnew;
        }
    }
    /* printf("z = %f, t = %f\n",z1,t1); */
    /* t = approximate location of the root*/
}

if (*valid) {
    if (polarization == TEmode) {
        *delta = pi/2.0 - acos(nprTE*sin(asin(nfTE*sin(t1)/nprTE)-alphapr));
        /* printf("delta(TE mode %d) = %f\n",mode,*delta*180.0/pi); */
    }
    else {
        *delta = pi/2.0 - acos(nprTM*sin(asin(nfTM*sin(t1)/nprTM)-alphapr));
        /* printf("delta(TM mode %d) = %f\n",mode,*delta*180.0/pi); */
    }
}
}

```